



# Atypical stability of exsolved Ni-Fe alloy nanoparticles on double layered perovskite for CO<sub>2</sub> dry reforming of methane

Xueli Yao<sup>a,1</sup>, Qingpeng Cheng<sup>b,1</sup>, Yerrayya Attada<sup>a</sup>, Samy Ould-Chikh<sup>a</sup>, Adrian Ramírez<sup>a</sup>, Xueqin Bai<sup>a</sup>, Hend Omar Mohamed<sup>a</sup>, Guanxing Li<sup>b</sup>, Genrikh Shterk<sup>a</sup>, Lirong Zheng<sup>c</sup>, Jorge Gascon<sup>a,d</sup>, Yu Han<sup>a,b</sup>, Osman M. Bakr<sup>a</sup>, Pedro Castaño<sup>a,d,\*</sup>

<sup>a</sup> KAUST Catalysis Center (KCC), King Abdullah University of Science and Technology (KAUST), Thuwal 23955-6900, Saudi Arabia

<sup>b</sup> Advanced Membranes and Porous Materials Center, Physical Sciences and Engineering Division, King Abdullah University of Science and Technology (KAUST), Thuwal 23955-6900, Saudi Arabia

<sup>c</sup> Beijing Synchrotron Radiation Facility, Institute of High Energy Physics, Chinese Academy of Sciences, Beijing 100049, PR China

<sup>d</sup> Chemical Engineering Program, Physical Science and Engineering (PSE) Division, King Abdullah University of Science and Technology (KAUST), Thuwal 23955-6900, Saudi Arabia

## ARTICLE INFO

### Keywords:

Coking resistant  
Dry reforming of methane  
Exsolution  
Ni-Fe alloy  
Perovskite oxide

## ABSTRACT

Dry reforming of methane simultaneously achieves several sustainability goals: valorizing methane-activating carbon dioxide while producing syngas. The catalyst has an enormous influence on the process viability by controlling activity, selectivity, and stability. A catalyst with uniform-sized Ni-Fe alloy nanoparticles anchored into PrBaMn<sub>1.6</sub>Ni<sub>0.3</sub>Fe<sub>0.1</sub>O<sub>5+δ</sub> double-layered perovskite is assembled via a facile one-step reduction strategy. Our method attains more exsolved Ni nanoparticles (94 %) than the common conditions. The exsolved Ni<sub>0.15</sub>Fe<sub>0.05</sub> catalyst shows exceptional stability in 260 h tests at 800 °C, with one of the slowest coke formation rates compared with the state-of-the-art catalysts. Besides, no deactivation was observed during 40 h operation at more demanding and coking conditions (14 bar) where this process is more likely to operate industrially. Via experimental characterizations and computational calculations, the stability of the robust exsolved Ni-Fe catalyst is demonstrated by its unique balance of adsorbed species, which inhibits coking.

## 1. Introduction

Due to the growing concern of the greenhouse gas reduction and the discovery of surplus shale gas reservation, the dry reforming of methane (DRM) reaction has attracted widespread attention [1–7]. The dry reforming of methane (DRM) is a prospective process to convert two major greenhouse gases, carbon dioxide (CO<sub>2</sub>) and methane (CH<sub>4</sub>), into syngas. The methane consumption in DRM is half of the steam reforming and partial oxidation reforming of methane [5]. It could potentially alleviate the adverse influence of these pollutants while supplying widely consumed chemicals [8–10]. The syngas produced in the reaction has a stoichiometric ratio of molecular hydrogen (H<sub>2</sub>) to carbon monoxide (CO) of 1:1, so to obtain a more favorable ratio, such as that for Fischer–Tropsch synthesis (2:1), we must cope by implementing such processes as steam reforming (3:1) or autothermal reforming (2.5:1) [11]. The problem is that these two processes have a very negative

carbon footprint, and it can be more efficient to trap carbon and raise the H<sub>2</sub>:CO ratio by taking advantage of the reactivity of CO [12,13]. Moreover, the ratio can be lower with a subsequent reverse water-gas shift reaction. The rest of the reactions involved in the process are the Boudouard and CH<sub>4</sub> decomposition [14]. One of the critical elements in this reaction is the catalyst stability, which depends on various factors, including coking [15,16]. The stability of the catalyst plays a role that could be more important than the activity per se [17].

Among the long list of catalysts used and tested for this process, nickel (Ni)-supported catalysts stand out for their balanced cheap price and high activity from an industrial point view [18]. However, these catalysts greatly suffer from severe coking and thermal sintering due to their low Tammann temperature [19–22]. Hence, the development of Ni-based catalysts with superior activity and stability sparked numerous catalysis studies. Many factors impact the sintering and coking resistance of the Ni-based catalysts, such as particle size, the strong metal

\* Corresponding author at: KAUST Catalysis Center (KCC), King Abdullah University of Science and Technology (KAUST), Thuwal 23955-6900, Saudi Arabia.

E-mail address: [pedro.castano@kaust.edu.sa](mailto:pedro.castano@kaust.edu.sa) (P. Castaño).

<sup>1</sup> These authors contributed equally to this work.

support interactions (SMSI), surface oxygen species and lattice oxygen in the support, surface carbonate species and the formation of alloy. Reducing the particle size will provide more active sites and suppress the carbon deposition [23]. The SMSI highly improves the dispersion of Ni particles and alleviate the possibility of sintering, leading to the enhancement of the activity and preventing coking [24–26]. Significant studies by Kawi's group have demonstrated that both surface and lattice oxygen species were investigated to play a key role in activating the C-H bond of CH<sub>4</sub> molecule and carbon suppression [27–29]. The lattice oxygen could react with CO<sub>2</sub>, forming monodentate and bidentate carbonate, which alleviates the carbon deposition by oxidation of surface carbon and exhaust as CO [30]. In addition, alloying with a second metal, altering the geometric and electronic structure of Ni active site, will achieve an optimized synergetic effect, enhancing the activity, selectivity, and stability [31]. Due to the inherent scientific significance and crucial role in technology view, bimetallic alloys have obtained widespread appeal [32]. In this case, the goal is to change the electron density of the Ni atoms by inducing additional metal, affecting the typically considered rate-determining step: CH<sub>4</sub> dissociation [33]. The alloy formed between the Ni and second metal can improve the stability, alleviating the coke deposition (e.g., noble metals are known to enhance the stability of Ni-based catalysts) [34]. A promising approach to enhance the performance of Ni-supported catalysts without affecting the price that much is to use a secondary metal, such as iron (Fe), cobalt (Co), copper (Cu), or molybdenum (Mo) [31,35]. Moreover, Fe is very interesting due to its low cost and synergistic effect upon intimate interaction with Ni [36,37].

The support and its integration with the metal also play a crucial role in catalyst activity, selectivity, and stability [38]. Conventionally, the synthesis, such as wet impregnation or vapor deposition, lacks control of particle size, dispersion, morphology, and metal-support interaction, leading to faster sintering and coking [39–41]. The in situ exsolution on perovskites overcomes these problems, improving the metal-support interactions and stabilizing the Ni exsolved particles [42–46]. In this method, the transition metal cations partially substitute the perovskite oxide (ABO<sub>3</sub>) B-site cations, then migrate (exsolve) from the host lattice and agglomerate in the form of nanoparticles under reduction conditions [47,48].

Among the investigated perovskites in the exsolution concept, A-site ordered double-layer perovskite system PrBaMn<sub>2</sub>O<sub>5+δ</sub> has drawn significant attention in solid oxide fuel cells due to its thermal and chemical stability, high oxygen diffusion rate, appreciable catalytic activity in hydrocarbon oxidation and the high flexibility to regulate first-row transition metal in the B sites as the active sites [49,50]. All these features benefit the performance of the catalyst under harsh DRM conditions. In DRM, several studies have investigated this type of perovskite with Ni with an 11 % CH<sub>4</sub> conversion at 800 °C and 5 h on stream with little coke deposition (0.017 g<sub>coke</sub> g<sub>cat</sub><sup>-1</sup> h<sup>-1</sup>) [51]; or with Co-Mo with a CO<sub>2</sub> conversion higher than 95 % at 800 °C and 24 h on stream [52]. To avoid most metal cations remaining embedded in the host bulk, resulting in low metal utilization, Joo et al. [53] performed systematic research on the perovskite by adopting the topotactic exsolution approaches in which guest cation was first supported on the matrix perovskite and then ion exchanged with the exsolved cation. The multi-step strategy improved the B-site transition metal exsolved fractions compared to typical conditions, which was applied to catalyst systems such as Ni-Fe [54], Co-Fe [55], and Co-Ni-Fe [56], to facilitate more exsolved nanoparticles, all of which displayed enhanced catalytic activity. However, novel strategies need to be explored and developed aiming a larger fraction of exsolved metal in a facile way. In addition, the enhancements of the stability and fundamental understanding of the deactivation mechanisms over these exsolved catalyst systems need to be clarified too.

Firstly, we aim to explore and develop new methods to exsolve a high fraction of Ni and Ni-Fe alloy and make uniform-sized metal nanoparticles anchored into a stoichiometric PrBaMn<sub>1.6</sub>Ni<sub>0.4-2x</sub>Fe<sub>2x</sub>O<sub>5+δ</sub>

double-layer perovskite. Secondly and given the intimate interaction between the nanoparticles and the support, our goal is to understand the reasons behind the potential higher stability (slower coking and sintering) in worst case scenarios: long term reactions and at high pressure. To this aim, we will combine several catalyst formulations with variable proportions of Ni and Fe in PrBaMn<sub>1.6</sub>Ni<sub>0.4-2x</sub>Fe<sub>2x</sub>O<sub>5+δ</sub> matrix with fixed ratios of Pr, Ba, and Mn, preparation methods, and characterization techniques, including x-ray absorption spectroscopy, dry reforming reactions and ab initio calculations. We will determine the fine structure of the catalyst responsible for the potential higher stability of the catalyst.

## 2. Experimental

### 2.1. Catalyst preparation

A series of Pr<sub>0.5</sub>Ba<sub>0.5</sub>Mn<sub>0.8</sub>Ni<sub>0.2-x</sub>Fe<sub>x</sub>O<sub>3</sub> ( $x = 0, 0.05, 0.1, 0.2$ ), defined as P-Ni<sub>0.2-x</sub>Fe<sub>x</sub> was synthesized using the improved sol-gel method. Stoichiometric Pr(NO<sub>3</sub>)<sub>3</sub>·6 H<sub>2</sub>O (Aldrich, 99.9 %, metal basis), Ba(NO<sub>3</sub>)<sub>2</sub> (Aldrich, 99 %), Mn(NO<sub>3</sub>)<sub>2</sub>·4 H<sub>2</sub>O (Aldrich, 98 %), Ni(NO<sub>3</sub>)<sub>2</sub>·6 H<sub>2</sub>O (Aldrich, 98.5 %), and Fe(NO<sub>3</sub>)<sub>3</sub>·9 H<sub>2</sub>O (Aldrich, 98 %) were dissolved in distilled water. The appropriate amounts of citric acid (Aldrich 99.5 %) and ethylene glycol (Aldrich) were added into the solutions as complexation agents, adjusting the mole ratio of metal ion to citric acid to ethylene glycol as 1:3:1.5. The pH value of the solution was maintained at around 8 by adding ammonium hydroxide. The resulting aqueous solution was continuously stirred at 85 °C forming a uniform gel, which was heated at 350 °C to decompose slowly and completely. Then, the precursor powder was ground and calcined at 950 °C for 4 h in air. After reduction pretreatment, the single layer perovskite transformed to double layered PrBaMn<sub>1.6</sub>Ni<sub>0.4-2x</sub>Fe<sub>2x</sub>O<sub>5+δ</sub>, defined as E-Ni<sub>0.2-x</sub>Fe<sub>x</sub>. A sequence of Pr<sub>0.5</sub>Ba<sub>0.5</sub>Mn<sub>1-x</sub>Ni<sub>x</sub>O<sub>3</sub> ( $x = 0, 0.1, 0.3$ ), defined as E-Ni<sub>x</sub>, was also prepared with the same procedure to investigate the effect of the Fe promoter. In contrast, the corresponding Ni-impregnated Pr<sub>0.5</sub>Ba<sub>0.5</sub>MnO<sub>3</sub> was prepared via the wetness impregnation method. Regarding the wetness impregnation method, a Pr<sub>0.5</sub>Ba<sub>0.5</sub>MnO<sub>3</sub> perovskite support, prepared with the same process mentioned above, was impregnated with a proper amount of Ni(NO<sub>3</sub>)<sub>2</sub>·6 H<sub>2</sub>O (Aldrich, 98.5 %) solution. And then the slurry was dried overnight at 80 °C, calcined at 350 °C for 2 h and at 950 °C for 4 h, respectively to achieve the Pr<sub>0.5</sub>Ba<sub>0.5</sub>MnO<sub>3</sub>/Imp Ni<sub>x</sub> ( $x = 0.1, 0.2, 0.3$ ) samples, defined as Syn-I-Ni<sub>x</sub>. After reduction pretreatment, the perovskite support in Pr<sub>0.5</sub>Ba<sub>0.5</sub>MnO<sub>3</sub>/Imp Ni<sub>x</sub> transformed to double layered perovskite in PrBaMn<sub>2</sub>O<sub>5+δ</sub>/Imp Ni<sub>x</sub>, defined as I-Ni<sub>x</sub>. The chemical composition of the prepared materials and their abbreviations are presented in Table S1. The nominal and actual loading of different catalysts are presented in Table S2.

### 2.2. Catalyst characterization

The XRD was performed using a Bruker D8 Advanced A25 diffractometer in Bragg-Brentano geometry equipped with a Cu K $\alpha$  target ( $\lambda = 1.54056 \text{ \AA}$ ) at 40 kV and 40 mA in the range of 10° to 80° under continuous scanning mode. The N<sub>2</sub> adsorption-desorption measurement was performed to analyze the specific surface area with a Micromeritics ASAP 2020 surface area and porosity analyzer by collecting the nitrogen sorption isotherms at 77 K, from which the specific surface area was calculated according to the Brunauer-Emmett-Teller equation.

Thermogravimetric analysis and differential thermogravimetric measurements of the fresh samples were conducted in 5 % H<sub>2</sub>/N<sub>2</sub> from 25 °C to 800 °C at a heating rate of 10 °C min<sup>-1</sup> using the Mettler-Toledo Star system. The thermogravimetric analysis mass spectrometry was conducted under temperature-programmed oxidation to study the amount and type of C deposited on the catalysts. The used catalysts were heated to 800 °C at 10 °C min<sup>-1</sup> in 10 % molecular oxygen (O<sub>2</sub>)/argon (Ar).

The reducibility of the perovskites was investigated by the H<sub>2</sub>

temperature-programmed reduction using a Micromeritics AutoChem II 2920 chemisorption analyzer. Before the measurement to remove the absorbed impurities, 100 mg sample was pretreated at 300 °C for 1 h with Ar and then cooled to 50 °C. After switching the gas flow to 10 % H<sub>2</sub>/Ar, the H<sub>2</sub> consumption was monitored with a thermal conductivity detector during heating the temperature from 150 °C to 850 °C at 10 °C min<sup>-1</sup>. Moreover, a cold trap made of ice was set between the sample and detector to remove the water formed during the process.

The oxygen temperature-programmed desorption (O<sub>2</sub>-TPD) was also conducted with the Micromeritics AutoChem II 2920 chemisorption analyzer. The samples were first pre-reduced at 800 °C with 10 % H<sub>2</sub>/Ar for 6 h and then in-situ reduced for 30 min in AutoChem. After flushing the sample with He at the sample temperature for 30 min, the system cooled down to 50 °C in He. Then the sample was treated with 20 % O<sub>2</sub>/N<sub>2</sub> at 50 °C for 30 min. After flushing the sample with He for 1 h, the O<sub>2</sub>-TPD was performed by increasing the temperature from 50 °C to 800 °C in 40 mL min<sup>-1</sup> He with a ramp of 10 °C min<sup>-1</sup>.

The morphology of the samples was observed using scanning electron microscopy (SEM; FEI Teneo VS) at an accelerated voltage of 5 kV. The sample was deposited on graphite and sputtered with a gold (Au) conductive layer. The sample TEM was performed using a Cs-Probe corrected Titan microscope from Thermo Fisher Scientific. It operated at the accelerating voltage of 300 kV and with a 0.5–0.8 nA beam current. Dark-field imaging was performed by STEM coupled with a HAADF detector. The STEM-HAADF data were acquired with a convergence angle of 21.4 mrad and a HAADF inner angle of 49 mrad.

Furthermore, an x-ray energy-dispersive spectrometer (FEI SuperX, ≈0.7 sr collection angle) was also employed with dark-field STEM imaging to acquire STEM-EDS spectrum-imaging datasets (dwell time 2.5 μs). A corresponding EDS spectrum was obtained during the acquisition of these datasets to generate the elemental maps at every image pixel. After background subtraction, the elemental maps for Ni, Fe, Mn, Pr, Ba, and O atoms were computed using the extracted intensity of their respective Kα or Lα lines. The generated maps were slightly post-filtered by applying a Gaussian filter (sigma = 0.5). The STEM electron energy loss spectroscopy (EELS) analysis was performed by operating the microscope at the accelerating voltage of 300 kV using a convergence angle of 17 mrad and an effective collection angle of 36 mrad. The spectrum-imaging dataset included the simultaneous acquisition of zero-loss and core-loss spectra (DualEELS) using a 0.5 eV/channel dispersion. It was recorded using a beam current of 0.2 nA and a 5 ms pixel<sup>-1</sup> dwell time. The Fe L<sub>2,3</sub>-edge, Ni L<sub>2,3</sub>-edge, and O K-edge were selected to build the chemical maps. Plural scattering was removed from the Fe and Ni L-edges using Fourier-ratio deconvolution with prior energy shift correction and background subtraction (power-law model). The contribution of transitions from the 2p<sup>3/2</sup> and 2p<sup>1/2</sup> initial states to the continuum states must be considered to acquire the white-line intensities of the L<sub>3</sub> and L<sub>2</sub> edges. The latter was conducted through a classical normalization with the Athena software [57]. Then, the L-edge spectra were modeled with a double arctangent step function and two split Lorentzian functions to account for the peak asymmetry [58]. The white-line intensities were finally computed from the area of the Lorentzian peaks.

The x-ray absorption spectroscopy of the prepared and reduced catalysts was performed at the 1W1B beamline at the Beijing Synchrotron Radiation Facility. The catalysts were ex-situ reduced for XAS analysis. The fresh catalysts were first pressed into pellets and reduced under the corresponding gas conditions. And then, the reduced pellets were collected and sealed in a glove box. Afterward, the sealed pellets were tested. The data were collected in the transmission mode via a Si (111) double crystal monochromator, detuned to reject higher harmonics. In addition, the Ni (8333 eV) and Fe (7113 eV) standard foils were applied for energy calibration. The Ni foil, NiO, Fe foil, FeO, and Fe<sub>2</sub>O<sub>3</sub> were used as references to analyze the XANES and EXAFS. The as-obtained XAFS data were processed using the Athena software program.

The XPS was conducted to investigate the chemical surface composition using a Kratos Axis Ultra DLD spectrometer equipped with a

monochromatic aluminum Kα x-ray source ( $h\nu = 1486.6$  eV). The XPS spectra were referenced to the C1s binding energy of 284.6 eV. The fitting of the XPS peaks was processed using XPSPEAK software.

The Raman analysis of the used catalysts was performed on an RXN1 Raman spectrometer (Kaiser Optical Systems) fitted with a 532 nm laser operating at 40 mW. In addition, inductively coupled plasma-optical emission spectrometry was performed to analyze the exact elemental content using an Agilent 5100 instrument. Before the measurement, the materials were digested in an ETHOS1 microwave digestion milestone.

In-situ diffuse reflectance infrared Fourier transform spectroscopy (in-situ DRIFTS) was conducted in a Nicolet 6700 IR spectrophotometer (Thermo Scientific) equipped with a Harrick Praying Mantis DRIFTS gas cell. Before the measurements, the catalysts were pre-reduced at 800 °C for 6 h in a quartz tube and then reduced in situ in the DRIFTS cell at 450 °C for 1 h, followed by flushing with He flow. The background was collected under a He flow at 450 °C. Gas-switching experiments (step 1 (He flow after CH<sub>4</sub>) → step 2 (CO<sub>2</sub> flow) → step 3 (mix gas flow: CH<sub>4</sub>/CO<sub>2</sub>/N<sub>2</sub> = 33/34/33)) were carried out at 450 °C to unravel the evolution characteristics of surface species on the catalysts. The time-resolution IR spectra were recorded in a range of 400–4000 cm<sup>-1</sup> at 32 scans per spectrum and 4 cm<sup>-1</sup> resolution with an interval of 30 s

### 2.3. Dry reforming of methane

Catalytic tests were performed in a four-channel Flowrence XD platform from Avantium. The reactors are 300-mm-long quartz tubes, of which the outside and inside diameters are 3 and 2 mm, respectively. One of the reactors was adopted as the blank without a loading catalyst among the four channels. Typically, 10 mg catalyst was loaded in a quartz reactor, and the gas flow was 5 mL min<sup>-1</sup> for each reactor. The catalysts were pelletized and sieved to achieve a powder with sizes between 150 and 250 μm. The proper amount of catalyst and reactant mixture gas flow was used to maintain the gas hourly space velocity (GHSV) per channel at 30,000 mL g<sub>cat</sub><sup>-1</sup> h<sup>-1</sup> under atmospheric pressure and 12,000 mL g<sub>cat</sub><sup>-1</sup> h<sup>-1</sup> under high pressure at 14 bar, respectively. The composition of the reactant mixture gas is CH<sub>4</sub>:CO<sub>2</sub>:N<sub>2</sub> = 33 %:34 %:33 %. Prior to feeding the reactant gas, the catalysts were reduced in situ in a 10 % H<sub>2</sub>/Ar atmosphere for 6 h at 800 °C. The reactants and products were continuously monitored with an online micro gas chromatograph (Agilent 7890B).

The conversions of *i* (CH<sub>4</sub> or CO<sub>2</sub>) were calculated as:

$$X_i = F_i^{\text{inlet}} - F_i^{\text{outlet}} / F_i^{\text{inlet}} \quad (1)$$

Where  $F_i^{\text{inlet}}$  and  $F_i^{\text{outlet}}$ , denote the inlet and outlet molar flow rate of *i*. The apparent rates of reaction are calculated as follows:

$$-r_{i,\text{app}} = F_i^{\text{inlet}} X_i / (W_{\text{Ni}}) \quad (2)$$

Where *W* is the catalyst loading and *W*<sub>Ni</sub> is the nickel loading. The H<sub>2</sub>/CO ratio is defined as:

$$\text{H}_2/\text{CO} = F_{\text{H}_2}^{\text{outlet}} / F_{\text{CO}}^{\text{outlet}} \quad (3)$$

The apparent coke formation rate ( $r_{\text{coke}}|_{\text{app}}$  in mmol g<sub>cat</sub><sup>-1</sup> s<sup>-1</sup>) was evaluated via temperature-programmed oxidation (TPO) combined with MS experiments. The coke formation rate was calculated based on Eq. (4).

$$r_{\text{coke}}|_{\text{app}} = f_{\text{coke}}/t \quad (4)$$

Where  $f_{\text{coke}}$  represents the amount of coke formed on the catalyst in mmol g<sub>cat</sub><sup>-1</sup> considering coke as pure carbon, at a given time on stream (*t*).

The thermodynamic equilibrium conversions of CH<sub>4</sub> and CO<sub>2</sub> and the H<sub>2</sub>/CO ratio were determined by Aspen Plus software.

### 2.4. Theoretical calculations

Adsorption energy calculations were performed with the first-

principles DFT using the Vienna Ab Initio Simulation Package (VASP). The electron exchange and correlation interactions were modeled using the generalized gradient approximation with the Perdew–Burke–Ernzerhof functional. The electron-ion interactions were defined using the projector-augmented wave method. A plane-wave basis set was used to describe the valence electrons with an energy cut-off of 400 eV. The Brillouin zone, sampled at the Monkhorst-Pack  $3 \times 3 \times 1$  k-point grid, was used as the Ni (111) and  $\text{Ni}_4\text{Fe}_1$  (111) model. The Ni (111) and  $\text{Ni}_4\text{Fe}_1$  (111) surfaces were modeled as a four-layer slab using a  $5 \times 5$  supercell with 15 Å of vacuum between the slabs. All geometries were optimized until the convergence reached  $1.0 \times 10^{-6}$  eV, and the atomic forces were smaller than  $0.05 \text{ eV } \text{\AA}^{-1}$ . For the gas phase molecule, a cubic box of  $15 \times 15 \times 15 \text{ \AA}^3$  was used. The climbing image nudged-elastic band method was used to identify the transition state structures of the elementary reactions involved in the reaction mechanisms. The following equation was used to calculate the binding energy of species present in the reaction media:

$$E_{\text{Bind}} = E_{\text{adsorbate+surface}} - E_{\text{adsorbate}} - E_{\text{surface}}, \quad (5)$$

where  $E_{\text{adsorbate+surface}}$  is the total energy of the adsorbate on the metal surface, and  $E_{\text{adsorbate}}$  and  $E_{\text{surface}}$  denote the total energy of adsorbate in the gas phase and the bare metal surface, respectively. A more negative binding energy value refers to the species adsorbed stronger on the metal surface (or a stronger interaction between the adsorbate and the metal site of the surface), and vice versa.

### 3. Results and discussion

#### 3.1. Structural characterization

The crystalline structures of the parent  $\text{PrBaMn}_2\text{O}_{5+\delta}$  perovskite (P) and the corresponding exsolved counterparts  $\text{P-Ni}_{0.2-x}\text{Fe}_x$  ( $x = 0, 0.05, 0.1, 0.2$ ) with different Ni/Fe loading were analyzed using x-ray diffraction (XRD) before and after reduction (Fig. 1). Moreover, the

crystalline structures of varying Ni substitution amounts for Mn have also been investigated (Fig. S1). The parent and exsolved materials comprise a perovskite structure with a mixture of hexagonal and cubic phases (Fig. 1a). However, the reduction induced the transformation of the original perovskite into a layered perovskite in the tetragonal phase (Fig. 1b), which might increase the specific surface area due to the formation of metal (Ni or Ni-Fe alloy) nanoparticles on the support surface and defects in the lattice (Fig. S2) [49].

For  $\text{P-Ni}_{0.2}$ , the diffraction peak located at  $44.5^\circ$  is attributed to metallic Ni due the exsolution [59,60]. Concerning  $\text{P-Ni}_{0.15}\text{Fe}_{0.05}$ , the similar diffraction peak shifts slightly to a lower diffraction degree, assigned to the diffraction peak of Ni-Fe alloy (Fig. 1c), deriving from Fe dissolving into the Ni lattice, revealing that the exsolved metal forms a binary Ni-Fe alloy [54]. Upon reduction, the exsolved nanoparticles in B sites are MnO for P, metallic Ni for  $\text{P-Ni}_{0.2}$ , and Ni-Fe alloy for  $\text{P-Ni}_{0.15}\text{Fe}_{0.05}$  and  $\text{P-Ni}_{0.1}\text{Fe}_{0.1}$ . The composition of the exsolved Ni-Fe alloy varies according to the Fe substitution since the increase of the Fe content in the matrix relatively decreases the exsolved Ni amount. Combined with the following TEM analysis, from  $\text{E-Ni}_{0.15}\text{Fe}_{0.05}$  to  $\text{E-Ni}_{0.1}\text{Fe}_{0.1}$ , the exsolved Ni-Fe alloy composition varied from  $\text{Ni}_4\text{Fe}_1$  to  $\text{Ni}_3\text{Fe}_1$ . In contrast, no exsolved Fe phase is evident for  $\text{P-Fe}_{0.2}$  (Fig. 1c). The same trend of transition metal exsolution in the layered perovskite was previously observed, indicating that Ni exsolves more efficiently to the surface than Mn and Fe [48]. The results demonstrate that, although Fe alone hardly exsolves, the existence of Ni in the B site promotes the exsolution of Fe, forming a Ni-rich Ni-Fe alloy nanoparticle.

The dynamic exsolution process was evaluated by analyzing the weighted loss profiles (through thermogravimetry, Fig. 2a and b),  $\text{H}_2$  consumption (through the thermal conductivity detector, Fig. 2c) and SEM (Fig. S3) during the reduction and exsolution processes. For the  $\text{P-Ni}_{0.2-x}\text{Fe}_x$  materials, three peaks are observed at (i)  $250\text{--}450^\circ\text{C}$ , attributed to the loss of oxygen in the  $\text{PrO}_x$  plane; (ii)  $450\text{--}650^\circ\text{C}$ , attributed to the partial escape of the intensely bonded lattice oxygen atoms from the perovskite [61]; and (iii) above  $650^\circ\text{C}$ , attributed to the

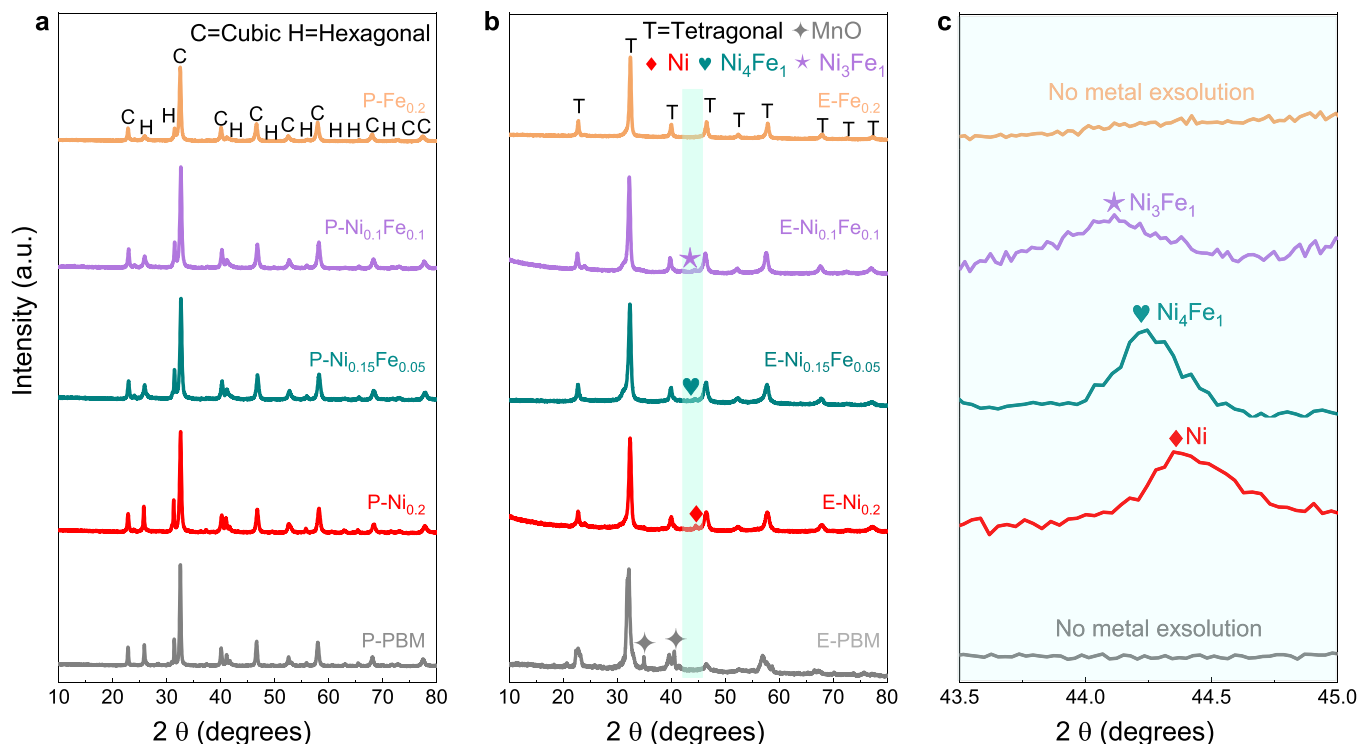


**Fig. 1.** X-ray diffraction patterns of perovskites and catalysts before and after reduction. (a) Parent (P) and  $\text{P-Ni}_{0.2-x}\text{Fe}_x$  ( $x = 0, 0.05, 0.1, 0.2$ ) after sintering at  $950^\circ\text{C}$  for 4 h in air. (b) P and  $\text{P-Ni}_{0.2-x}\text{Fe}_x$  ( $x = 0, 0.05, 0.1, 0.2$ ) after reduction at  $800^\circ\text{C}$  in 10 %  $\text{H}_2/\text{Ar}$  for 6 h. (c) Refined XRD spectrum with smaller step size between the range marked with a cyan rectangle.



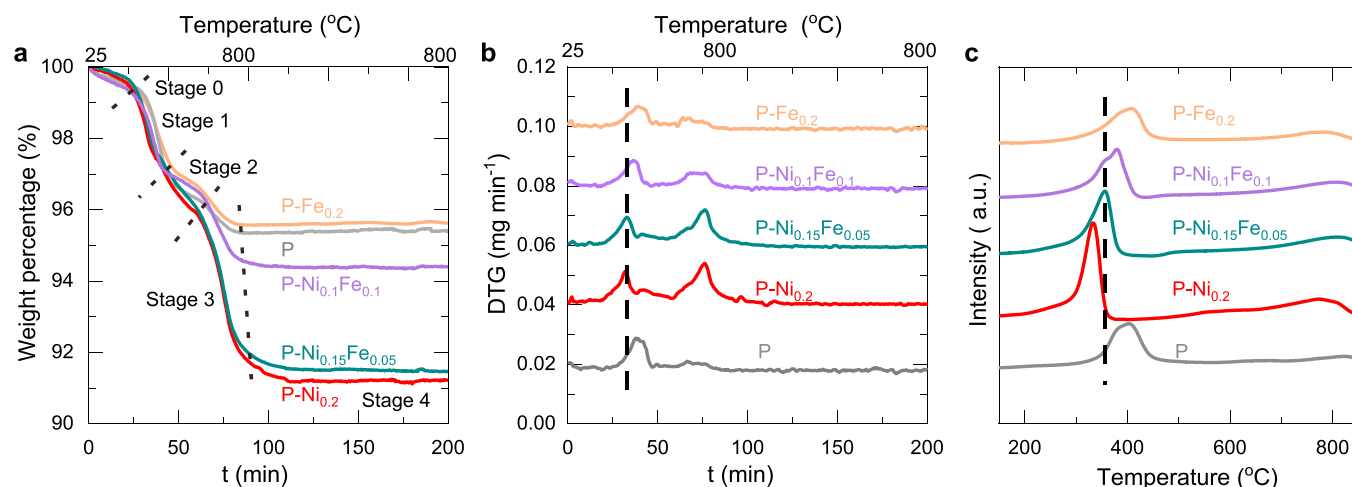


**Fig. 2.** Dynamic exsolution process of P and  $\text{P-Ni}_{0.2-x}\text{Fe}_x$  ( $x = 0, 0.05, 0.1, 0.2$ ) catalysts: (a) thermogravimetric analysis (b) differential thermogravimetric (DTG) measurements in 5 %  $\text{H}_2/\text{N}_2$ . (c)  $\text{H}_2$  temperature-programmed reduction patterns in 10 %  $\text{H}_2/\text{Ar}$ .

reduction of metal cations located at the B site and the exsolved process of Ni or Ni-Fe to the double-layer perovskite surface. A higher Ni content in the perovskite triggered a lower reduction temperature of the first peak due to the higher electronegativity of Ni (1.75) compared to Mn

(1.69) [62]. As Ni is more reducible than Fe, from  $\text{P-Ni}_{0.2}$  to  $\text{P-Fe}_{0.2}$ , the reaction peak shifts to a higher temperature, and the hydrogen consumption decreases in sequence with the increase in the Fe.

The exsolution of the nanoparticles was observed from the

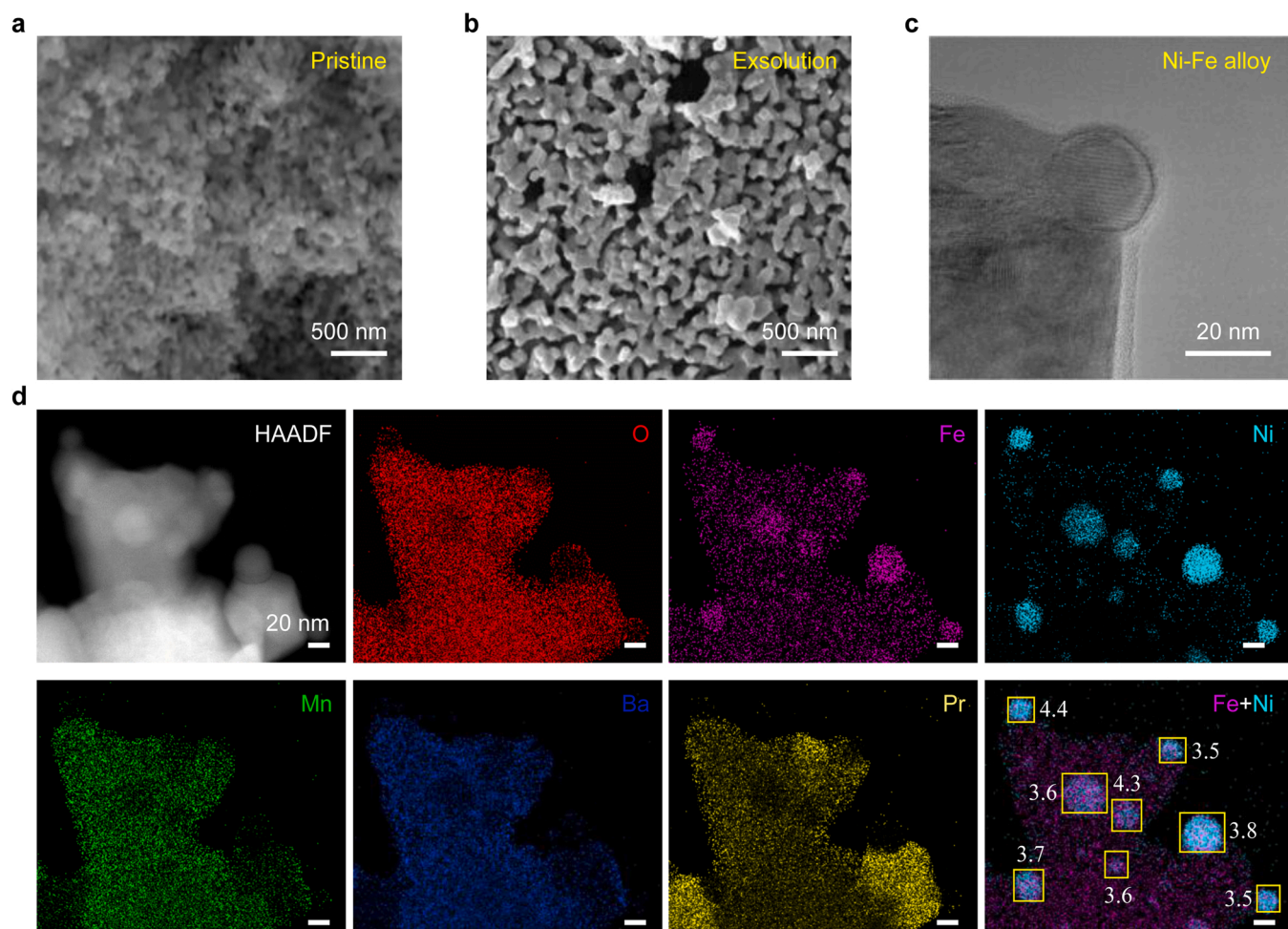


**Fig. 3.** Micro morphology of  $\text{P-Ni}_{0.15}\text{Fe}_{0.05}$  before and after reduction. (a) Scanning electron microscopy (SEM) of pristine  $\text{P-Ni}_{0.15}\text{Fe}_{0.05}$  and (b) SEM and (c) transmission electron microscopy (TEM) of  $\text{E-Ni}_{0.15}\text{Fe}_{0.05}$ . (d) High-angle annular dark-field scanning TEM (STEM) imaging and elemental mappings computed from STEM-energy dispersive x-ray spectroscopy data for the  $\text{E-Ni}_{0.15}\text{Fe}_{0.05}$  catalyst (after  $\text{H}_2$ -reduction). The yellow box marked the selected nanoparticles. The Ni/Fe ratio of the marked nanoparticles are determined with EDX analysis.

morphology of the P-Ni<sub>0.15</sub>Fe<sub>0.05</sub> material. High-angle annular dark-field (HAADF) scanning transmission electron microscopy (STEM) and energy-dispersive x-ray spectroscopy (EDS) elemental mapping were performed to confirm the composition of the exsolved nanoparticles and support. The pristine P-Ni<sub>0.15</sub>Fe<sub>0.05</sub> material has a homogeneous porous surface (Fig. 3a), whereas numerous nanoparticles emerged on the surface after H<sub>2</sub> treatment (Fig. 3b). A detail of an exsolved nanoparticle that was partially socketed in the support is shown Fig. 3c. The results shown in Fig. 3d indicate the spherical shape of the Ni-Fe particles anchored to the surface of the double-layer perovskite. The interplanar spacing of the nanoparticles is 2.05 Å, which is consistent with the d-spacing of the (111) plane of the Ni-Fe alloy phase (Fig. S4) [37]. The particle size analysis of the E-Ni<sub>0.15</sub>Fe<sub>0.05</sub> catalyst indicates an average of 21 ± 5.6 nm. The EDS elemental mappings highlight that only Ni and Fe atoms were found in the emergent nanoparticles. The quantitative analysis of the EDS data operated on more than 30 nanoparticles indicated a molar Ni/Fe ratio of 3.6 ± 1.0. The chemical elements Pr, Ba, Mn, and O are homogeneously distributed across the support. Only traces of Ni atoms remained in the perovskite, whereas a substantial number of Fe atoms were still present, in agreement with the calculations by Kwon et al. [48]. The same exsolution phenomenon of Ni-Fe and Ni nanoparticles was also observed for E-Ni<sub>0.1</sub>Fe<sub>0.1</sub> (Figs. S5 and S6) and E-Ni<sub>0.2</sub> (Fig. S7), respectively.

The local coordination environment and chemical state of the exsolved nanoparticles were further analyzed using x-ray absorption fine structure spectroscopy (XAFS) at the Ni and Fe K-edges of E-Ni<sub>0.2</sub> and E-Ni<sub>0.15</sub>Fe<sub>0.05</sub> catalysts. Even though the reduced pellets were handled carefully during the transfer and test process, it could not be excluded that slight surface oxidation could occur. In the normalized Ni

K-edge x-ray absorption near-edge structure (XANES) spectra (Fig. 4a), the Ni K-edge spectra almost fit with the Ni foil reference concerning the energy position and pattern, indicating that Ni is prevalently reduced to Ni<sup>0</sup> in the two catalysts. In addition, the pre-edge peak slightly shifts to higher energy from E-Ni<sub>0.2</sub> to E-Ni<sub>0.15</sub>Fe<sub>0.05</sub> (an enlarged region in Fig. 4a), demonstrating the minor increase in the Ni average oxidation state, indicating the formation of the Ni-Fe alloy [56].

Moreover, the white line (7131 eV) of the Fe K-edge XANES spectrum of the E-Ni<sub>0.15</sub>Fe<sub>0.05</sub> catalyst is more intense than that of Fe foil in Fig. 4b, indicating that part of the Fe is oxidized [63]. The intensity of the pre-edge peak of E-Ni<sub>0.15</sub>Fe<sub>0.05</sub> is stronger than that of the Fe<sub>2</sub>O<sub>3</sub> reference. Thus, it is deduced that part of the Fe is reduced to metallic Fe<sup>0</sup>, whereas another part remains oxidized in the double-layer perovskite support. The wavelet transform signals of the Ni-metal bond were observed around 8 Å<sup>-1</sup> in the contour plots of the E-Ni<sub>0.15</sub>Fe<sub>0.05</sub>, E-Ni<sub>0.2</sub>, NiO reference, and Ni foil. In contrast, the Ni-O bond signals were absent except for the NiO standard (Fig. 4c and Fig. S8). In addition, Fig. 4d and e exhibit the extended XAFS (EXAFS) spectra in the k-space and the corresponding Fourier transform in the R space at the Ni K-edges. The monometallic E-Ni<sub>0.2</sub> reveals the same oscillations as those of the Ni foil, whereas in terms of the bimetallic E-Ni<sub>0.15</sub>Fe<sub>0.05</sub>, the changes minor shift to a smaller k-value. The slight k-value shifted for the bimetallic Ni-Fe system is reported by previous work [36]. The EXAFS spectra of both E-Ni<sub>0.2</sub> and E-Ni<sub>0.15</sub>Fe<sub>0.05</sub> have similar characteristics to those of Ni foils, with the Ni-Ni coordination at ~2.18 Å (Fig. 4e). This result confirms the existence of Ni in the metallic state [64].

The linear combination fitting (LCF) method was adopted based on the identifiable features of each reference in the XANES spectra to quantify the distribution of different Ni and Fe oxidation states. The LCF

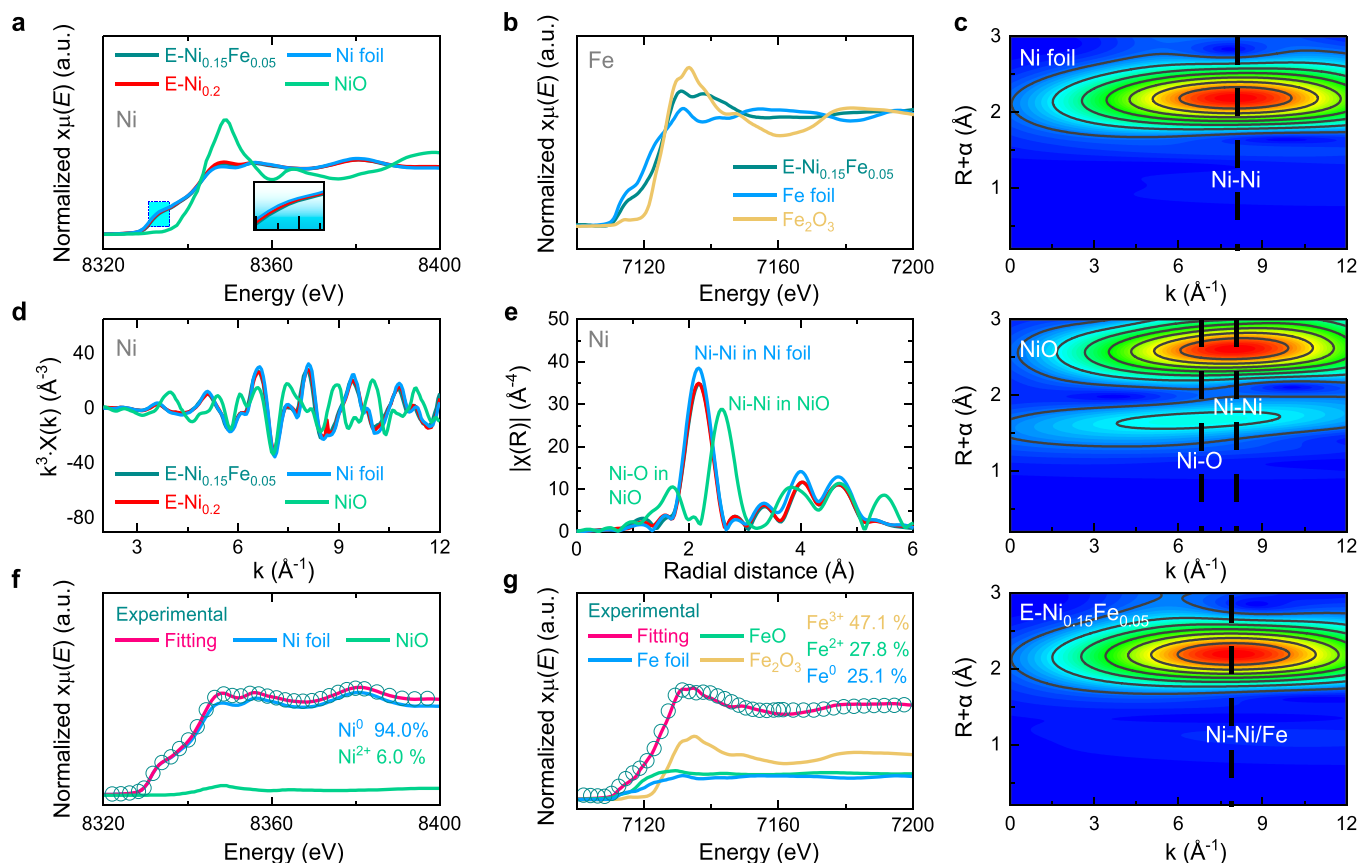


**Fig. 4.** Synchrotron x-ray absorption fine structure (XAFS) measurement of various catalysts. (a) Normalized Ni K-edge x-ray absorption near-edge structure (XANES) spectra, (b) normalized Fe K-edge XANES spectra, (c) wavelet transform EXAFS plots of Ni foil, NiO, and E-Ni<sub>0.15</sub>Fe<sub>0.05</sub>; (d) corresponding  $k^3$ -weighted Ni K-edge extended XAFS (EXAFS) spectra in  $k$  spaces, (e) Fourier transform of  $k^3$ -weighted Ni K-edge EXAFS for E-Ni<sub>0.15</sub>Fe<sub>0.05</sub> and E-Ni<sub>0.2</sub>, (f) Ni K-edge, and (g) Fe K-edge with linear combination fitting of the E-Ni<sub>0.15</sub>Fe<sub>0.05</sub>.

analysis of the Ni K-edge XANES spectrum reveals that about 94.0 % of Ni is reduced to the metallic state, which is almost double the other reported results (58 % Ni exsolved) [48], and only 6.0 % of Ni remains in the oxidation state in E-Ni<sub>0.15</sub>Fe<sub>0.05</sub> (Fig. 4f). However, the distribution of Fe in E-Ni<sub>0.15</sub>Fe<sub>0.05</sub> is approximately 25.1 % Fe<sup>0</sup> and 74.9 % in the Fe oxidation state (Fig. 4g).

The x-ray photoelectron (XPS) spectra of the fresh catalyst (Fig. 5a) indicate that only divalent Ni<sup>2+</sup> (~854.5 eV, 856.6 eV) and satellite peaks (~860.8 eV) are detected in P-Ni<sub>0.15</sub>Fe<sub>0.05</sub> [65]. The metallic nickel Ni<sup>0</sup> peaks (~852.3 eV) appeared after reduction (Fig. 5b), accounting for only a small fraction of the Ni elements, most likely due to oxidation during ex situ movement. Similar to Ni, the Fe element exhibits mixed oxidation states consisting of Fe<sup>2+</sup> (~709.6 eV) and Fe<sup>3+</sup> (~710.8 eV) before reduction (Fig. 5d), a small part of which is reduced to Fe<sup>0</sup> (706.7 eV) after reduction treatment (Fig. 5e) [66]. The XPS spectra indicate that metallic Ni<sup>0</sup> and Fe<sup>0</sup> coexist in the E-Ni<sub>0.15</sub>Fe<sub>0.05</sub> catalyst, further implying the formation of Ni-Fe alloy. The oxygen species consists of lattice oxygen (~528.5 eV) and adsorbed oxygen species (~531 eV) as shown in Fig. S9a and b. The peak ratio of the adsorbed/lattice oxygen increases on the E-Ni<sub>0.15</sub>Fe<sub>0.05</sub> surface with respect to that on the P-Ni<sub>0.15</sub>Fe<sub>0.05</sub> surface [67], which is ascribed to the formation of oxygen vacancies along with the Ni-Fe alloy exsolution process [68].

Thus, combined with the XRD (Fig. 1), TEM (Fig. 3), and XAFS analysis (Fig. 4), we infer that Fe was partially reduced to the metallic phase and exsolved to the surface of the perovskite matrix, forming an alloy with Ni [59].

### 3.2. Catalytic performance

The catalytic activity and stability of the preceding impregnated (I-) and exsolved (E-) catalysts were evaluated in dry reforming at 800 °C under atmospheric pressure and high pressure (14 bar). The activity of the catalysts is compared based on the apparent reaction rates of CH<sub>4</sub> and CO<sub>2</sub>. The amount of Ni in the normalized activity is obtained by ICP. This term is considered “apparent” because it is derived from any value of conversion, including the ones of the integral reactor ( $X > 10\%$ ). Although it is not convenient to refer to it as an “intrinsic reaction rate”, it provides us with a parameter that can be used to compare activity across our catalysts and those of the literature.

The initial apparent reaction rate of CH<sub>4</sub> for exsolved catalysts (E-Ni<sub>x</sub>,  $x = 0.1, 0.2$ , and  $0.3$ ) are much higher than those of their impregnated counterparts (I-Ni<sub>x</sub>; Fig. 6a). Moreover, unlike the fast deactivation of the impregnated catalyst, even the most stable I-Ni<sub>0.2</sub> catalyst in the impregnated catalysts dropped by 11.5 % within 12 h (Fig. 6a), the E-Ni<sub>x</sub> catalysts remain stable for the CH<sub>4</sub> reaction rate throughout 40 h on stream, mirroring the same stability as the H<sub>2</sub>/CO ratio (Fig. S10). As for the effect of the Ni loading, the apparent reaction rate of E-Ni<sub>x</sub> catalysts decreased as the amount of Ni increases, despite the conversion delivered opposite trend (Fig. S10).

Based on the results, E-Ni<sub>0.2</sub> is further modified with the dopant of Fe in the B site (E-Ni<sub>0.2-x</sub>Fe<sub>x</sub> ( $x = 0.05, 0.1, 0.2$ )). The CH<sub>4</sub> apparent reaction rate of the E-Ni<sub>0.15</sub>Fe<sub>0.05</sub> catalyst is slightly lower than that of the E-Ni<sub>0.2</sub> (Fig. 6a and b). The CH<sub>4</sub> apparent reaction rate of the E-Ni<sub>0.1</sub>Fe<sub>0.1</sub> catalyst is not stable during 40 h on stream. For E-Fe<sub>0.2</sub>, its catalytic performance results show negligible CH<sub>4</sub> and CO<sub>2</sub> apparent reaction

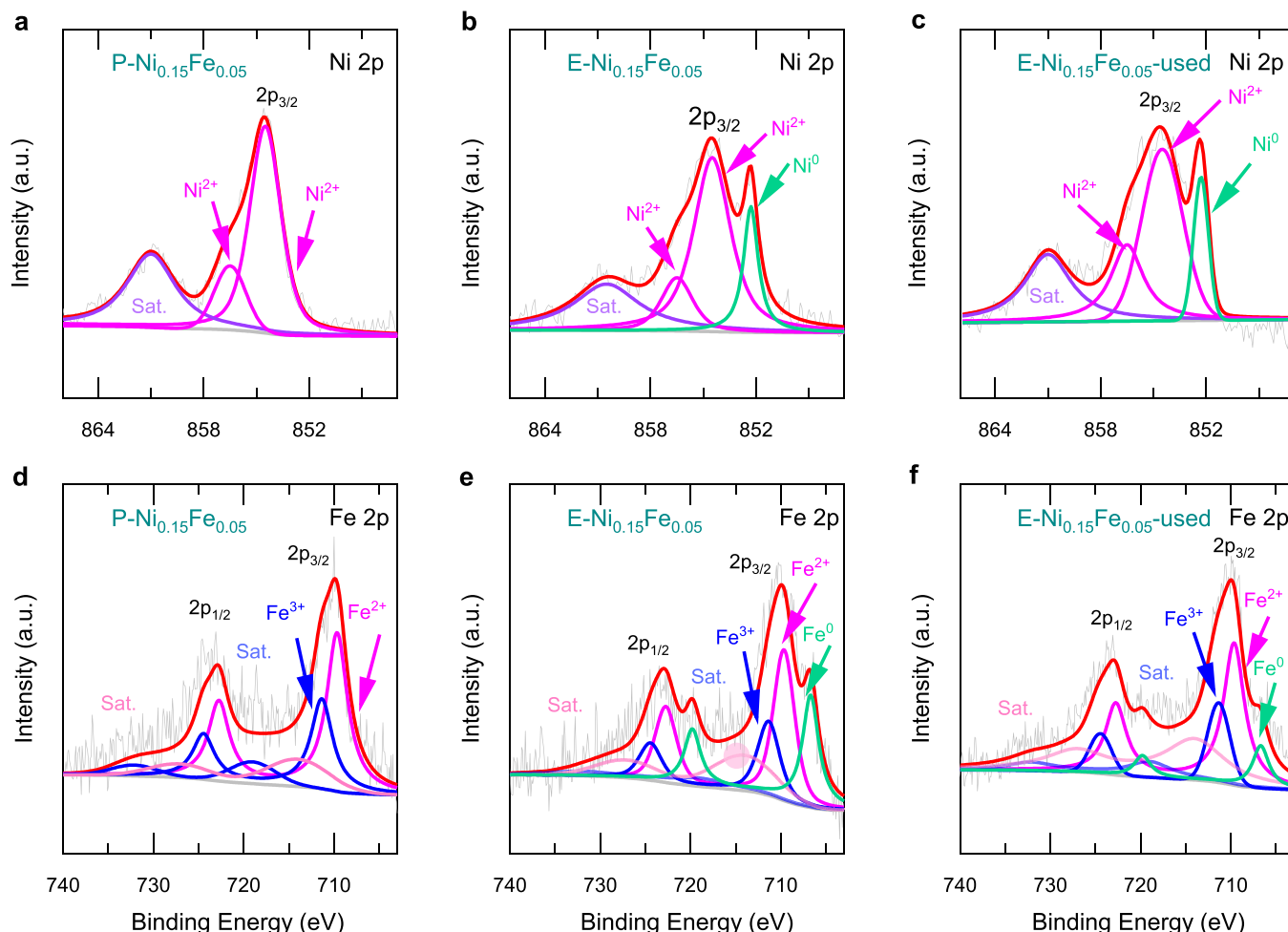
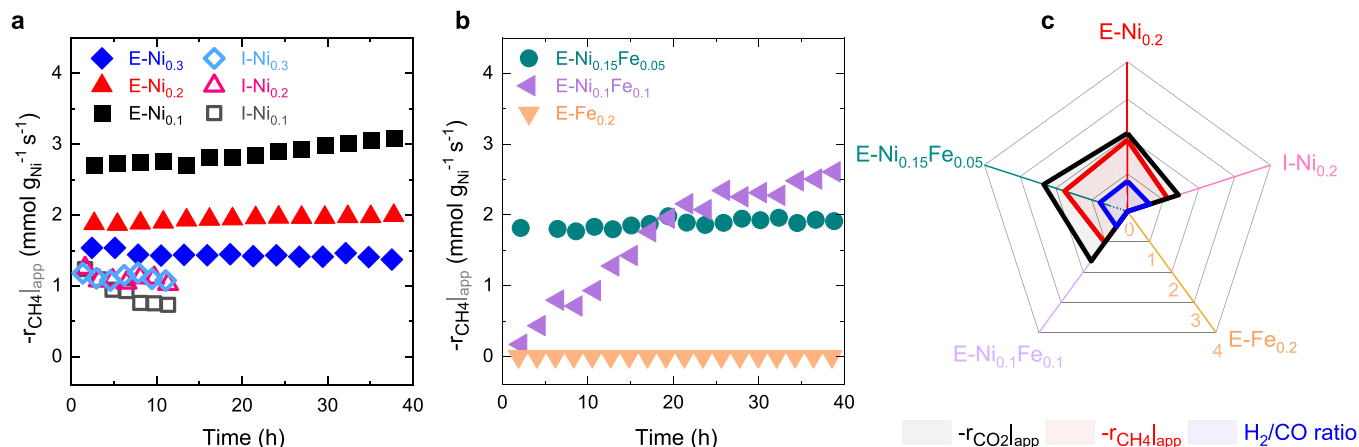


Fig. 5. X-ray photoelectron spectra of P-Ni<sub>0.15</sub>Fe<sub>0.05</sub>, E-Ni<sub>0.15</sub>Fe<sub>0.05</sub>, and used E-Ni<sub>0.15</sub>Fe<sub>0.05</sub>: (a, b, and c) Ni 2p, (d, e, and f) Fe 2p.



**Fig. 6.** Dry reforming of methane (DRM) activity of different catalyst. a, b, CH<sub>4</sub> reaction rate based on per gram Ni, (a) E-Ni<sub>x</sub> ( $x = 0.1, 0.2, 0.3$ ) and I-Ni<sub>x</sub> ( $x = 0.1, 0.2, 0.3$ ) samples, (b) E-Ni<sub>0.2-x</sub>Fe<sub>x</sub> ( $x = 0.05, 0.1, 0.2$ ) samples. (c) Activity comparison of E-Ni<sub>0.2-x</sub>Fe<sub>x</sub> ( $x = 0, 0.05, 0.1, 0.2$ ) and I-Ni<sub>0.2</sub> catalysts after a 12 h test. Reaction conditions:  $T = 800\ ^\circ C$ ,  $CH_4/CO_2/N_2 = 33/34/33$ ,  $GHSV = 30,000\ mL\ g_{cat}^{-1}\ h^{-1}$ .

rate, indicating that both the perovskite substrate and Fe nanoparticles are not active site for the conversion of CH<sub>4</sub> (Figs. 6b and S11), in agreement with the previous reports [69]. The CO<sub>2</sub> conversions are slightly higher than the corresponding CH<sub>4</sub> conversions for all catalysts,

independent of the metal loading and the Ni/Fe ratio (Figs. 6 and 7), probably originating from the reverse water-gas shift reaction (RWGS) [56,59]. RWGS usually occurs as a side reaction in DRM, which results in higher CO<sub>2</sub> conversion than CH<sub>4</sub> conversion and makes the H<sub>2</sub>/CO ratio

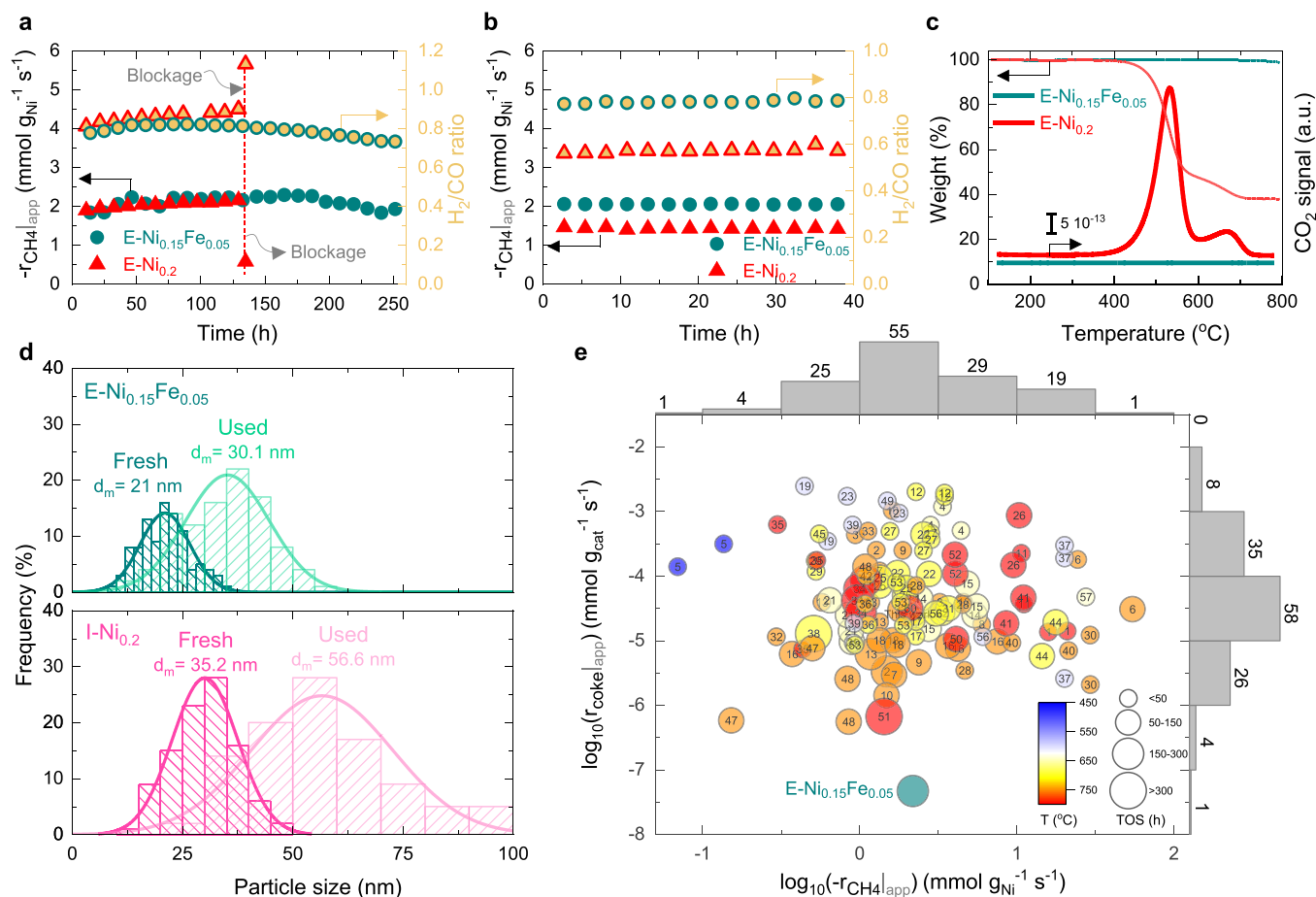


**Fig. 7.** Dry reforming of methane (DRM) performance of E-Ni<sub>0.2</sub> and E-Ni<sub>0.15</sub>Fe<sub>0.05</sub> catalysts and analysis of used catalysts. (a) Continuous catalytic reaction for 260 h during DRM. Reaction conditions:  $T = 800\ ^\circ C$ ,  $CH_4/CO_2/N_2 = 33/34/33$ ,  $GHSV = 30,000\ mL\ g_{cat}^{-1}\ h^{-1}$ . (b) High-pressure testing at 14 bar. Reaction conditions:  $T = 800\ ^\circ C$ ,  $CH_4/CO_2/N_2 = 20/60/20$ ;  $12,000\ mL\ g_{cat}^{-1}\ h^{-1}$  ( $1500\ h^{-1}$ ). (c) Thermogravimetric analysis of used E-Ni<sub>0.2</sub> (135 h) and E-Ni<sub>0.15</sub>Fe<sub>0.05</sub> catalysts (260 h) after different times on stream at  $800\ ^\circ C$  in 10 % O<sub>2</sub>/Ar. (d) Particle size distribution histogram calculated using Image J for E-Ni<sub>0.15</sub>Fe<sub>0.05</sub> and I-Ni<sub>0.2</sub> catalysts after reduction and DRM with different times on stream. (e) Comparison of the performance of the catalyst studied in this work at  $800\ ^\circ C$  with the catalysts used in dry reforming of methane (DRM) over the last years, based on methane apparent reaction rate ( $-r_{CH_4|app}$ ) and apparent coking rate ( $r_{coke|app}$ ) over different catalysts, temperatures and time on streams. The number in each point corresponds to a reference indicated in the Table S3.



lower than 1 since the reaction produces more CO and consumes H<sub>2</sub> [70]. The RWGS is observed in our catalysts in the results presented in Figs. S10–15 and corroborated by previous works [32,70]. Besides, compared to the exsolved catalyst, the unreduced E-Ni<sub>0.15</sub>Fe<sub>0.05</sub> catalyst without the generation of exsolved metal species synthesized by the same method exhibited relatively low activity and deactivated fast within 15 h (Fig. S12). Similarly, the E-Ni<sub>0.15</sub>Fe<sub>0.05</sub> catalyst reduced under pure H<sub>2</sub> at 800 °C also displayed low performance, probably due to the perovskite decomposition under pure H<sub>2</sub> (Fig. S13).

The long-term stability test for the E-Ni<sub>0.15</sub>Fe<sub>0.05</sub> and E-Ni<sub>0.2</sub> catalysts is presented in Fig. 7a and Fig. S14. After around 135 h on stream, the stability test of E-Ni<sub>0.2</sub> ceases because the catalyst bed is congested with coke (the pressure drop rises and the flow rate decreases). The E-Ni<sub>0.15</sub>Fe<sub>0.05</sub> catalyst displays a stable apparent reaction rate with no noticeable deactivation for 260 h on stream at 800 °C. This result indicates that Fe plays a critical role in stabilizing the catalyst. Besides, the E-Ni<sub>0.15</sub>Fe<sub>0.05</sub> catalyst shows 100 h stability under undilute gas conditions with CH<sub>4</sub>:CO<sub>2</sub> = 1:1 as feed gas without deactivation (Fig. S15). Industrial syngas must be compressed, such as compression from 1 to 10 bars, for utilization, which costs more than 85 % of the total capital investment and 60 % of the operational costs [71]. Additionally, the high-pressure operation increases the production capacity, as well. However, coking is highly favored in high-pressure conditions, which is the central dilemma to address. Both E-Ni<sub>0.15</sub>Fe<sub>0.05</sub> and E-Ni<sub>0.2</sub> exhibited 40 h stability in reaction conditions at 14 bar (Fig. 7b). Compared to a previous study [71], E-Ni<sub>0.15</sub>Fe<sub>0.05</sub> exhibits similar CH<sub>4</sub> conversion, lower CO<sub>2</sub> conversion, and a much higher H<sub>2</sub>/CO ratio (Fig. S16), even without 10 % H<sub>2</sub>O feeding, indicating that E-Ni<sub>0.15</sub>Fe<sub>0.05</sub> is also a promising catalyst for the high-pressure dry reforming of CH<sub>4</sub>.

### 3.3. Unusual coking and sintering resistance

To elucidate the role of Fe on the carbon resistance of Ni-based catalysts under reaction conditions, thermogravimetric techniques were applied to measure the carbon deposition on the used catalyst. The CO<sub>2</sub> signal was analyzed in a mass spectrometer during combustion. As depicted in Fig. 7c, the apparent coke formation rate on the E-Ni<sub>0.2</sub> catalyst is  $2.57 \cdot 10^{-5} \text{ mmol g}_{\text{cat}}^{-1} \text{ s}^{-1}$  during the 135 h on stream, whereas the apparent coke formation rate significantly drops to  $4.71 \cdot 10^{-8} \text{ mmol g}_{\text{cat}}^{-1} \text{ s}^{-1}$  for the E-Ni<sub>0.15</sub>Fe<sub>0.05</sub> catalyst during the 260 h on stream. Compared with approximately 140 catalysts from the state-of-the-art references, the proposed E-Ni<sub>0.15</sub>Fe<sub>0.05</sub> catalyst has the slowest apparent coke formation rates of the relatively extensive catalyst portfolio (Fig. 7e and Table S3). Many studies in the literature do not assess coke fouling on the catalysts for the following reasons: (i) insufficient time on stream, (ii) unrealistically mild reaction conditions, or (iii) inappropriate excess of catalyst and the subsequent underestimation of coke formation. Per the thermogravimetric results, contrary to the severe coking on the used E-Ni<sub>0.2</sub> catalyst, the Raman spectra indicated no coke accumulation on the used E-Ni<sub>0.15</sub>Fe<sub>0.05</sub> catalyst (Fig. S17). The minor coking deposition convincingly demonstrates the coking-resistant effect of Fe, coinciding with previous reports that Fe substitution improves the coking resistance of Ni-based catalysts in reaction conditions [72]. In addition, the used catalyst after high-pressure conditions at 14 bar is also characterized and shown in Fig. S18. Generally, the high pressure favored the coking formation. The weight loss of the used E-Ni<sub>0.15</sub>Fe<sub>0.05</sub> is only 2 % after 40 h on stream. Compared to the used E-Ni<sub>0.2</sub>, the D and G band intensity of the used E-Ni<sub>0.15</sub>Fe<sub>0.05</sub> is lower, further indicating an improvement of coking resistance with the introduction of Fe even at high pressure.

The particle size distribution analysis revealed that the used E-Ni<sub>0.15</sub>Fe<sub>0.05</sub> catalyst possessed exsolved Ni-Fe nanoparticles with an average size of 30.1 nm after 260 h on stream, slightly larger than the nanoparticles of the E-Ni<sub>0.15</sub>Fe<sub>0.05</sub> before the reaction (21.0 nm; Fig. 7d). The exsolved nanoparticles of the used E-Ni<sub>0.15</sub>Fe<sub>0.05</sub> catalyst anchor partially in the support without any observable coke with a morphology

similar to the pristine one (Fig. S19a and c). However, the counterpart used I-Ni<sub>0.2</sub> catalyst exhibited severe sintering of Ni particles from 35.2 to 56.6 nm only after 12 h on stream with apparent filamentous coke on the catalyst surface (Fig. 7d, S19b and d). Hence, the exsolved E-Ni<sub>0.15</sub>Fe<sub>0.05</sub> catalyst exhibited improved sintering resistance compared with the I-Ni<sub>0.2</sub> catalyst, which is closely associated with their stability (Figs. 6 and 7).

Structural changes in the E-Ni<sub>0.15</sub>Fe<sub>0.05</sub> catalyst between the reduced state and after the reaction were further investigated using STEM coupled with electron energy loss spectroscopy (EELS). Spatially resolved EELS spectra at the L-edges were used to analyze the metal oxidation state in the core and particle surfaces. For 3d metals, a typical L-edge EELS spectrum includes a pair of strong white lines corresponding to  $2p^{3/2} \rightarrow 3d$  (L<sub>3</sub>-edge) and  $2p^{1/2} \rightarrow 3d$  (L<sub>2</sub>-edge) transitions and two edge jumps corresponding to  $2p \rightarrow \text{continuum}$  transitions. The two white lines are separated by the spin-orbit interaction of the 2p core states. A one-electron excitation theory usually fails to interpret the spectral fingerprint (e.g., branching ratio and multiple interactions) because the 2p- and 3d-hole have radial wave functions overlapping significantly [73].

In this work, we restrict the analysis of the L<sub>2,3</sub>-edges by considering only the total intensity of the white lines. Previous authors have demonstrated that the total number of 3d holes is proportional to the integrated L<sub>2,3</sub>-edge peaks (see experimental method section), which is a useful feature to determine the metal oxidation state [74–77]. Fig. 8 presents the Ni and Fe L-edge spectra of the metal and metal monoxide standards, with spectra taken in the core and shell of the Ni-Fe nanoparticles before and after the catalytic reaction. The comparison of the total intensities of the white lines with the Fe and Ni standards ( $I(\text{Fe}) = 21$  and  $I(\text{Ni}) = 10$ ) indicated that the nanoparticle core remains in a metallic state throughout the reaction ( $I(\text{Fe}) = 20$  and  $I(\text{Ni}) = 10$ –11). This result is in agreement with the XPS spectra of the used catalyst (Fig. 5c and f). For the oxidized shell of the used catalyst, the Ni atoms were in a mixture of Ni<sup>0</sup> and Ni<sup>2+</sup> states ( $I(\text{Ni}) = 16$  vs.  $I(\text{Ni}) = 23$  in NiO), whereas the Fe atoms were predominantly in the Fe<sup>2+</sup> state with a probable minor presence of the Fe<sup>3+</sup> state ( $I(\text{Fe}) = 32$  vs.  $I(\text{Fe}) = 29$  in FeO).

The same observations were made for the oxidized shell of the reduced catalyst. Thus, the presence of the latter oxide shell on metal nanoparticles was essentially due to handling the catalyst in the air prior to the TEM analysis. To eliminate these effects, the quasi in-situ TEM is performed in reaction conditions and displayed in Fig. S20. This result shows the partial redistribution of Fe and a relatively low concentration of oxygen layer surrounding the Ni-Fe nanoparticles in the E-Ni<sub>0.15</sub>Fe<sub>0.05</sub> catalyst. Thus, we can consider that as the initial status of the catalyst (before the reaction). In contrast, FeO<sub>x</sub> species are formed on the outer layer of the Ni-Fe alloy nanoparticles during the dry reforming conditions [78]. Besides, the average Ni/Fe molar ratio of 3.6 significantly increased to 9.2 after the reaction with a much larger standard deviation (from 1.0 to 5.3, measured on 38 particles). This evidence that part of the metallic iron was redistributed on the support during the reaction agrees with previous observations of Coperet et al. [63].

### 3.4. The mechanistic reason behind the slower coke formation

The DFT calculations were performed to compare the adsorption energy of the key intermediates on Ni<sub>4</sub>Fe<sub>1</sub> (111) models to that on monometallic Ni (111) models to elucidate the improved coking resistance of the Ni-Fe bimetallic catalyst at the atomic resolution level. These surfaces were considered as they were identified experimentally using XRD (Fig. 1c), high-resolution TEM (Figs. S4 and S7), EDX analysis (Fig. 3d), EELS analysis (Fig. 8). Even though the oxygen vacancy defects in the perovskite matrix will assist increasing ratios of singlet oxygen species on the surfaces for removing carbon species, the TGA and TPR results in a reduction atmosphere (as shown in Fig. 2) indicated that the amount of the oxygen vacancy originating from metal exsolution of P-

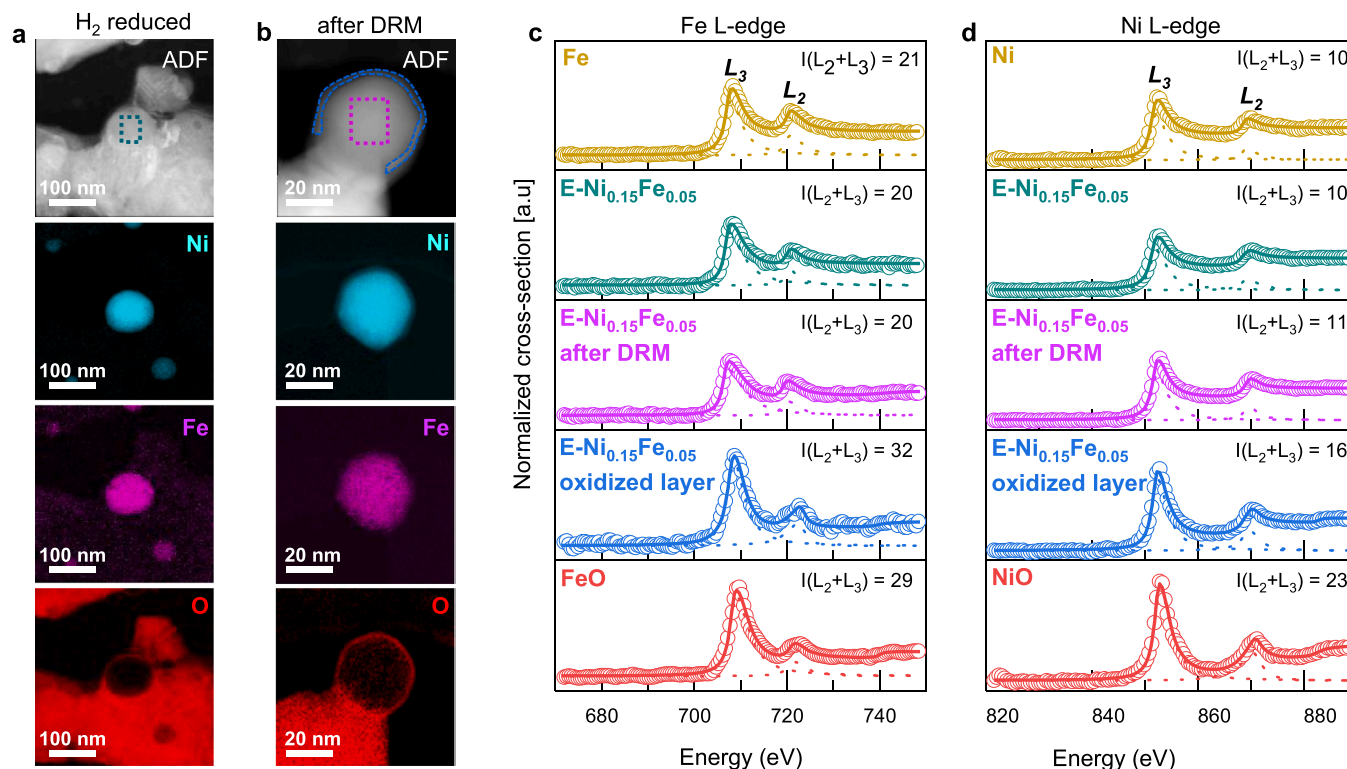


**Fig. 8.** Annular dark-field scanning transmission electron microscopy (STEM) imaging and elemental mappings computed from STEM electron energy loss spectroscopy (EELS) data for E-Ni<sub>0.15</sub>Fe<sub>0.05</sub> catalysts: (a) After H<sub>2</sub>-reduction and (b) dry reforming of methane at 800 °C. Green and purple boxes mark the core nanoparticle regions where the EELS spectra were extracted. The region outlined in blue was used to extract the EELS spectrum of the oxidized shell. The L-edge spectra of the oxidized shell correspond to an average of 10 extracted spectra of various points from this region. The Fe L-edge (c) and Ni L-edge spectra (d) of metal and metal monoxide standards are presented with the experimental spectra extracted from the colored boxes in (a) and (b). The open circles are experimental data. The full lines are fitted models, and the dotted lines are Lorentzian functions to model the white lines. The arctangent functions are not drawn for the sake of clarity. The parameter  $I(L_2 + L_3)$  corresponds to the total white-line intensity computed from the peak area of the Lorentzian function.

Ni<sub>0.2</sub> is slightly larger than that of P-Ni<sub>0.15</sub>Fe<sub>0.05</sub>. However, the coking resistance of E-Ni<sub>0.15</sub>Fe<sub>0.05</sub> is much better than that of E-Ni<sub>0.2</sub>, indicating that in these catalysts, the oxygen vacancy facilitates carbon removal, but it is not the main factor. Therefore, the effect of the perovskite support is not considered in the DFT calculations, which focused on elucidating the improvement of the coking resistance of E-Ni<sub>0.15</sub>Fe<sub>0.05</sub>. Thus, only the monometallic Ni and bimetallic Ni-Fe alloy were considered for the slab model (Figs. S21–S23). By calculating the effective barriers for the C and CH oxidation pathways on Ni and Ni<sub>4</sub>Fe<sub>1</sub> (111) surface (Fig. S24), it is considered that the O\* originating from the CO<sub>2</sub> dissociation directly oxidizes the intermediate CH\* is the dominant oxidation pathway on both Ni and Ni<sub>4</sub>Fe<sub>1</sub> (111) surfaces, which is consistent with other reports [36,81]. Although the slab model cannot conclude the fine structure of the Ni-Fe binary alloy, a reasonable understanding of the reaction mechanism was gained throughout the DFT.

The binding energies of the critical intermediates on Ni<sub>4</sub>Fe<sub>1</sub> (111) were compared with those on Ni (111), as presented in Table S4. Despite the same binding energy of CH<sub>4</sub> between Ni (111) and Ni<sub>4</sub>Fe<sub>1</sub> (111), the binding strength of carbon-containing intermediates, including CH<sub>3</sub>\*, CH<sub>2</sub>\*, CH\*, C\*, and CO\*, are all weaker on the Ni<sub>4</sub>Fe<sub>1</sub> (111) surface than that on the Ni (111) surface, on which coke is likely prone to form due to the higher C\* binding energy [82]. In addition, due to the stronger Fe–O bond, the adsorption of the oxygen-containing species, such as O\* and CHO\*, on the Ni<sub>4</sub>Fe<sub>1</sub> (111) surface is stronger than that on the Ni (111) surface, in agreement with the time-resolution DRIFTS spectra under switching gas conditions (Figs. S25 and S26) and previously reported results [36]. The O\* and CHO\* adsorption strengths on Ni<sub>4</sub>Fe<sub>1</sub> (111) surface are 0.15 and 0.08 eV higher than the pure Ni (111) surface. To observe the effects of Fe on the catalyst, the chemisorption energy of O, CO and C on pure Ni (111), Ni<sub>4</sub>Fe<sub>1</sub> (111) and pure Fe (111)

are plotted in Fig. 9a, b and c, respectively. The adsorption energy of O increases along with the increase of Fe composition, implying the oxophilic nature of Fe (Fig. 9a), consistent with the O<sub>2</sub>-TPD results (Fig. S27). In contrast, the adsorption energy of CO has no obvious correlation with the Fe composition (Fig. 9b). These trends indicate that the difference of CO<sub>2</sub> dissociation energy for various catalysts mainly originates from the adsorption capability of O\* species, instead of that of CO\* species (Fig. 9a and b). Besides, as shown in Fig. 9c, the adsorption energy of C closely connected with the Ni composition on the active site, further implying that coke prefers to form on pure Ni site other than Fe site.

In DFT calculations, we are mainly focusing on the coke formation reactions. The energy barriers of some key elementary steps of the reaction on Ni (111) and Ni<sub>4</sub>Fe<sub>1</sub> (111) surfaces are displayed in Figs. S24 and S28 and Table S5. The dissociative adsorption energies of CH<sub>4</sub> and CO<sub>2</sub> are presented in Fig. 9d and e. The CH<sub>4</sub> dissociation energy of Ni<sub>4</sub>Fe<sub>1</sub> is 0.04 eV higher than that of Ni (111), leading to less CH<sub>x</sub>\* (x = 0, 1, 2, 3) intermediate species on the Ni<sub>4</sub>Fe<sub>1</sub> (111) sites. Moreover, the CO<sub>2</sub> dissociation energy of Ni<sub>4</sub>Fe<sub>1</sub> (111) is 0.06 eV lower than that of pure Ni (111). Due to the oxophilic nature of Fe, adding Fe to Ni-based catalyst enhances the adsorption of O\* species and reduces the CO<sub>2</sub> dissociation energy (exhibiting a slightly inferior CH<sub>4</sub> dissociation energy compared to Ni). The higher concentration of O\* species on the surface of the Ni-Fe binary alloy catalyst reacts with C\* species and lower the coking rate, contributing to the atypical coking resistance of this catalyst.

#### 4. Conclusions

The direct exsolution of Ni and Ni-Fe in a single reduction step leads

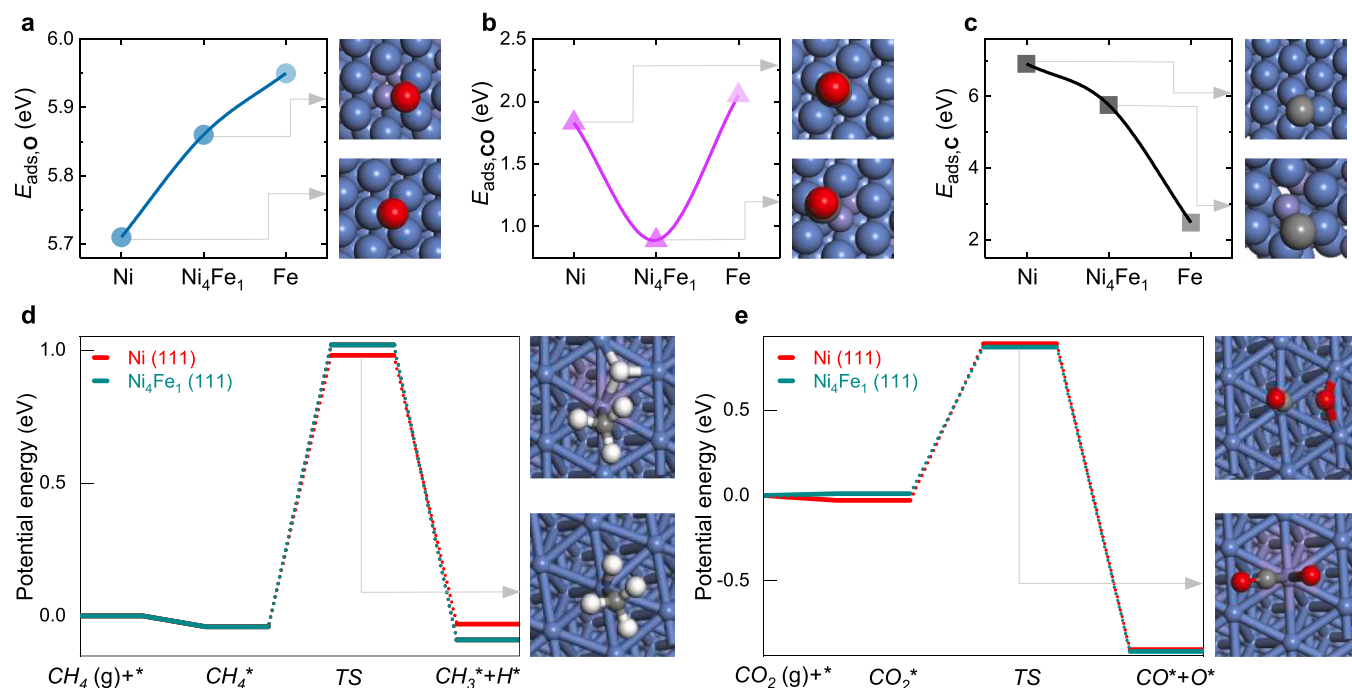


**Fig. 9.** Density function theory (DFT) calculations. (a, b and c) O, CO and C adsorption energies calculated on pure Ni (111), Ni<sub>4</sub>Fe<sub>1</sub> (111), and pure Fe (111) surfaces, respectively. The data points in lighter color in a [79] and b [80] are cited from the literature. (d) Potential energy profile for CH<sub>4</sub> dissociation and (e) CO<sub>2</sub> dissociation on Ni (111) and Ni<sub>4</sub>Fe<sub>1</sub> (111), respectively. Spheres: blue = Ni, purple = Fe, gray = C, white = H, and red = O.

to well dispersed, anchored and alloyed (in the case of the bimetallic sample) nanoparticles on PrBaMn<sub>1.6</sub>Ni<sub>0.4-2x</sub>Fe<sub>2x</sub>O<sub>5+δ</sub> double-layer perovskite. We synthesized these catalysts together with counterparts prepared by impregnation, characterized and tested them in the dry reforming of methane. The exsolved Ni-based catalyst has a significantly superior performance and longer stability due to enhanced metal-support interaction. The exsolved Ni-Fe alloy catalyst shows slightly slower reaction rates but a significantly longer lifetime: with negligible coke depositions at 800 °C during 260 h on stream under 1 bar or 40 h on stream under 14 bar (more relevant for industrial implementation). Our main objective has been to understand the reasons behind the higher stability of this Ni-Fe catalyst by characterization, ab initio calculations, and dry reforming reactions. Our results show that Fe (in the exsolved Ni-Fe catalyst) stabilizes O\* species, helps in the CO<sub>2</sub> dissociation, and facilitates the reactions of C\* species as its adsorption is weakened. At the same time, the stronger metal-support interaction in this catalyst leads to slower sintering. These combined effects are the reasons behind the atypical more extended stability of the exsolved Ni-Fe alloy catalyst.

#### CRedit authorship contribution statement

**Xueli Yao:** Conceptualization, Investigation, Methodology, Data curation, Writing – original draft, Writing – review & editing, Visualization. **Qingpeng Cheng:** Conceptualization, Methodology, Data curation, Writing – review & editing. **Yerrayya Attada:** DFT calculations and Formal analysis. **Samy Ould-Chikh:** Data curation, Formal analysis and Writing – review. **Adrian Ramirez:** Data curation and Formal analysis. **Xueqin Bai:** Investigation. **Hend Omar Mohamed:** Formal analysis. **Guanxing Li:** Data curation. **Genrikh Shterk:** Formal analysis. **Lirong Zheng:** Data curation and Formal analysis. **Jorge Gascon:** Formal analysis and review. **Yu Han:** Formal analysis and review. **Osman M. Bakr:** Formal analysis and review. **Pedro Castaño:** Funding acquisition, Project administration, Resources, Supervision, Formal analysis, Writing – review & editing.

#### Declaration of Competing Interest

The authors declare the following financial interests/personal relationships which may be considered as potential competing interests: Pedro Castano reports financial support was provided by King Abdullah University of Science and Technology. Pedro Castano has patent pending to King Abdullah University of Science and Technology (KAUST).

#### Data availability

Data will be made available on request.

#### Acknowledgements

This work was conducted thanks to the financial support of the King Abdullah University of Science and Technology (KAUST, BAS/1/1403).

#### Appendix A. Supporting information

Supplementary data associated with this article can be found in the online version at [doi:10.1016/j.apcatb.2023.122479](https://doi.org/10.1016/j.apcatb.2023.122479).

#### References

- [1] X.Y. Gao, K. Hidajat, S. Kawi, Facile synthesis of Ni/SiO<sub>2</sub> catalyst by sequential hydrogen/air treatment: A superior anti-coking catalyst for dry reforming of methane, *J. CO<sub>2</sub> Util.* 15 (2016) 146–153, <https://doi.org/10.1016/j.jcou.2016.05.007>.
- [2] X. Gao, H. Liu, K. Hidajat, S. Kawi, Anti-coking Ni/SiO<sub>2</sub> catalyst for dry reforming of methane: role of oleylamine/oleic acid organic pair, *ChemCatChem* 7 (2015) 4188–4196, <https://doi.org/10.1002/cctc.201500787>.
- [3] J. Ni, L. Chen, J. Lin, S. Kawi, Carbon deposition on borated alumina supported nano-sized Ni catalysts for dry reforming of CH<sub>4</sub>, *Nano Energy* 1 (2012) 674–686, <https://doi.org/10.1016/j.nanoen.2012.07.011>.
- [4] X.Y. Gao, J. Ashok, S. Widjaja, K. Hidajat, S. Kawi, Ni/SiO<sub>2</sub> catalyst prepared via Ni-aliphatic amine complexation for dry reforming of methane: Effect of carbon chain number and amine concentration, *Appl. Catal. A Gen.* 503 (2015) 34–42, <https://doi.org/10.1016/j.apcata.2015.07.005>.



- [5] X. Gao, Z. Lin, T. Li, L. Huang, J. Zhang, S. Askari, N. Dewangan, A. Jangam, S. Kawi, Recent developments in dielectric barrier discharge plasma-assisted catalytic dry reforming of methane over Ni-based catalysts, *Catalysts* 11 (2021), <https://doi.org/10.3390/catal11040455>.
- [6] Z. Bian, W. Zhong, Y. Yu, Z. Wang, B. Jiang, S. Kawi, Dry reforming of methane on Ni/mesoporous-Al<sub>2</sub>O<sub>3</sub> catalysts: Effect of calcination temperature, *Int. J. Hydrog. Energy* 46 (2021) 31041–31053, <https://doi.org/10.1016/j.ijhydene.2020.12.064>.
- [7] X. Gao, J. Li, M. Zheng, S. Cai, J. Zhang, S. Askari, N. Dewangan, J. Ashok, S. Kawi, Recent progress in anti-coking Ni catalysts for thermo-catalytic conversion of greenhouse gases, *Process Saf. Environ. Prot.* 156 (2021) 598–616, <https://doi.org/10.1016/j.psep.2021.10.051>.
- [8] D. Pakhare, J. Spivey, A review of dry (CO<sub>2</sub>) reforming of methane over noble metal catalysts, *Chem. Soc. Rev.* 43 (2014) 7813–7837, <https://doi.org/10.1039/c3cs60395d>.
- [9] L.C. Buelens, V.V. Galvita, H. Poelman, C. Detavernier, G.B. Marin, Super-dry reforming of methane intensifies CO<sub>2</sub> utilization via Le Chatelier's principle, *Science* 354 (80) (2016) 449–452, <https://doi.org/10.1126/science.aah7161>.
- [10] I.V. Yentekakis, P. Panagiotopoulou, G. Artemakis, A review of recent efforts to promote dry reforming of methane (DRM) to syngas production via bimetallic catalyst formulations, *Appl. Catal. B Environ.* 296 (2021), 120210, <https://doi.org/10.1016/j.apcatb.2021.120210>.
- [11] Y. Kathiraser, U. Oemar, E.T. Saw, Z. Li, S. Kawi, Kinetic and mechanistic aspects for CO<sub>2</sub> reforming of methane over Ni based catalysts, *Chem. Eng. J.* 278 (2015) 62–78, <https://doi.org/10.1016/j.cej.2014.11.143>.
- [12] C. Palmer, D.C. Upham, S. Smart, M.J. Gordon, H. Metiu, E.W. McFarland, Dry reforming of methane catalysed by molten metal alloys, *Nat. Catal.* 3 (2020) 83–89, <https://doi.org/10.1038/s41929-019-0416-2>.
- [13] M. He, Y. Sun, B. Han, Green carbon science: efficient carbon resource processing, utilization, and recycling towards carbon neutrality, *Angew. Chem. Int. Ed.* 61 (2022), e202112835, <https://doi.org/10.1002/anie.202112835>.
- [14] A. Gili, L. Schlicker, M.F. Bekheet, O. Görke, D. Kober, U. Simon, P. Littlewood, R. Schomäcker, A. Doran, D. Gaissmaier, T. Jacob, S. Selve, A. Gurlo, Revealing the mechanism of multiwalled carbon nanotube growth on supported nickel nanoparticles by in situ synchrotron x-ray diffraction, density functional theory, and molecular dynamics simulations, *ACS Catal.* 9 (2019) 6999–7011, <https://doi.org/10.1021/acscatal.9b00733>.
- [15] O. Daoura, G. Fornasieri, M. Boutros, N. El, P. Beaunier, C. Thomas, M. Selmane, A. Miche, C. Sassoie, O. Ersen, W. Baaziz, P. Massiani, A. Bleuzen, F. Launay, L. De Chimie, M. Lcpm, S. Li, C. Fanar, B.P. Jdeideh, One-pot prepared mesoporous silica SBA-15-like monoliths with embedded Ni particles as selective and stable catalysts for methane dry reforming, *Appl. Catal. B Environ.* 280 (2021), 119417, <https://doi.org/10.1016/j.apcatb.2020.119417>.
- [16] S. Das, A. Jangam, S. Jayaprakash, S. Xi, K. Hidajat, K. Tomishige, S. Kawi, Role of lattice oxygen in methane activation on Ni-phyllsilicate@Ce1-xZrO2 core-shell catalyst for methane dry reforming: Zr doping effect, mechanism, and kinetic study, *Appl. Catal. B Environ.* 290 (2021), 119998, <https://doi.org/10.1016/j.apcatb.2021.119998>.
- [17] I. Hita, S.M. Sarathy, P. Castaño, Polymeric waste valorization at a crossroads: ten ways to bridge the research on model and complex/real feedstock, *Green Chem.* 23 (2021) 4656–4664, <https://doi.org/10.1039/D1GC00845E>.
- [18] X. Li, D. Li, H. Tian, L. Zeng, Z.J. Zhao, J. Gong, Dry reforming of methane over Ni/La<sub>2</sub>O<sub>3</sub> nanorod catalysts with stabilized Ni nanoparticles, *Appl. Catal. B Environ.* 202 (2017) 683–694, <https://doi.org/10.1016/j.apcatb.2016.09.071>.
- [19] S. Kawi, Y. Kathiraser, J. Ni, U. Oemar, Z. Li, E.T. Saw, Progress in synthesis of highly active and stable nickel-based catalysts for carbon dioxide reforming of methane, *ChemSusChem* 8 (2015) 3556–3575, <https://doi.org/10.1002/cssc.201500390>.
- [20] U. Oemar, Y. Kathiraser, L. Mo, X.K. Ho, S. Kawi, CO<sub>2</sub> reforming of methane over highly active La-promoted Ni supported on SBA-15 catalysts: Mechanism and kinetic modelling, *Catal. Sci. Technol.* 6 (2016) 1173–1186, <https://doi.org/10.1039/c5cy00906e>.
- [21] L. Mo, K. Kai, M. Leong, S. Kawi, A highly dispersed and anti-coking Ni-La<sub>2</sub>O<sub>3</sub>/SiO<sub>2</sub> catalyst for syngas production from dry carbondioxide reforming of methane, *Catal. Sci. Technol.* (2014) 2107–2114, <https://doi.org/10.1039/c3cy00869j>.
- [22] X. Gao, J. Ashok, S. Kawi, A review on roles of pretreatment atmospheres for the preparation of efficient Ni-based catalysts, *Catal. Today* 397–399 (2022) 581–591, <https://doi.org/10.1016/j.cattod.2021.06.009>.
- [23] J. Ni, J. Zhao, L. Chen, J. Lin, S. Kawi, Lewis acid sites stabilized nickel catalysts for dry (CO<sub>2</sub>) reforming of methane, *ChemCatChem* 8 (2016) 3732–3739, <https://doi.org/10.1002/cctc.201601002>.
- [24] A. Pintar, Environmental Influence of active metal loading and oxygenmobility on coke-free dry reforming of Ni – Co bimetallic catalysts, *Appl. Catal. B Environ.* 125 (2012) 259–270, <https://doi.org/10.1016/j.apcatb.2012.05.049>.
- [25] K. Sutthiumporn, S. Kawi, Promotional effect of alkaline earth over Ni-La<sub>2</sub>O<sub>3</sub> catalyst for CO<sub>2</sub> reforming of CH<sub>4</sub>: role of surface oxygen species on H<sub>2</sub> production and carbon suppression, *Int. J. Hydrog. Energy* 36 (2011) 14435–14446, <https://doi.org/10.1016/j.ijhydene.2011.08.022>.
- [26] L. Yang, Y. Choi, W. Qin, H. Chen, K. Blinn, M. Liu, P. Liu, J. Bai, T.A. Tyson, M. Liu, Promotion of water-mediated carbon removal by nanostructured barium oxide/nickel interfaces in solid oxide fuel cells, *Nat. Commun.* 2 (2011), <https://doi.org/10.1038/ncomms1359>.
- [27] U. Oemar, K. Hidajat, S. Kawi, Role of catalyst support over PdO-NiO catalysts on catalyst activity and stability for oxy-CO<sub>2</sub> reforming of methane, *Appl. Catal. A Gen.* 402 (2011) 176–187, <https://doi.org/10.1016/j.apcata.2011.06.002>.
- [28] K. Sutthiumporn, T. Maneerung, Y. Kathiraser, S. Kawi, CO<sub>2</sub> dry-reforming of methane over La<sub>0.8</sub>Sr<sub>0.2</sub>Ni<sub>0.8</sub>MO<sub>2.0</sub> perovskite (M = Bi, Co, Cr, Cu, Fe): roles of lattice oxygen on C-H activation and carbon suppression, *Int. J. Hydrog. Energy* 37 (2012) 11195–11207, <https://doi.org/10.1016/j.ijhydene.2012.04.059>.
- [29] G. Editors, B.W. Jang, R. Glaser, C. Liu, B.W. Jang, R. Glaser, C. Liu, M.C. Capel-sanchez, J.M. Campos-martin, L.G. Fierro, E.E. Sci, A. Léonard, J.C. Rooke, C. F. Meunier, H. Sarmento, J. Descy, B. Su, B.G. Harvey, R.L. Quintana, J. Jae, G. A. Tompsett, Y. Lin, R. Torren, J. Shen, T. Zhang, B. Yang, E. Charles, W.C. Conner, G.W. Huber, Fuels of the Future Steam reforming of ethanol to H<sub>2</sub> over Rh / Y<sub>2</sub>O<sub>3</sub> : crucial roles of Y<sub>2</sub>O<sub>3</sub> oxidizing ability , space velocity , andH<sub>2</sub> / C, *Energy & Environmental Science* (2010) 2–3.
- [30] S. Das, A. Jangam, S. Jayaprakash, S. Xi, K. Hidajat, K. Tomishige, S. Kawi, Role of lattice oxygen in methane activation on Ni-phyllsilicate@Ce1-xZrO2 core-shell catalyst for methane dry reforming: Zr doping effect, mechanism, and kinetic study, *Appl. Catal. B Environ.* 290 (2021), 119998, <https://doi.org/10.1016/j.apcatb.2021.119998>.
- [31] Z. Bian, S. Das, M.H. Wai, P. Hongmanorom, S. Kawi, A review on bimetallic nickel-based catalysts for CO<sub>2</sub> reforming of methane, *ChemPhysChem* 18 (2017) 3117–3134, <https://doi.org/10.1002/cphc.201700529>.
- [32] S. Kawi, Y. Kathiraser, J. Ni, U. Oemar, Z. Li, Progress in synthesis of highly active and stable nickel-based catalysts for carbon dioxide reforming of methane, *ChemSusChem* (2015) 3556–3575, <https://doi.org/10.1002/cssc.201500390>.
- [33] Y. Lu, D. Guo, Y.Y. Zhao, P.S. Moyo, Y.Y. Zhao, S. Wang, X. Ma, Enhanced catalytic performance of Nix-V@HSS catalysts for the DRM reaction: the study of interfacial effects on Ni-VOx structure with a unique yolk-shell structure, *J. Catal.* 396 (2021) 65–80, <https://doi.org/10.1016/j.jcat.2021.02.005>.
- [34] S.A. Theofanidis, V.V. Galvita, M. Sabbe, H. Poelman, C. Detavernier, G.B. Marin, Controlling the stability of a Fe–Ni reforming catalyst: structural organization of the active components, *Appl. Catal. B Environ.* 209 (2017) 405–416, <https://doi.org/10.1016/j.apcatb.2017.03.025>.
- [35] Y. Song, E. Ozdemir, S. Ramesh, A. Adishev, S. Subramanian, A. Harale, M. Albulali, B.A. Fadhel, A. Jamal, D. Moon, S.H. Choi, C.T. Yavuz, Dry reforming of methane by stable Ni–Mo nanocatalysts on single-crystalline MgO, *Science* 367 (80) (2020) 777–781, <https://doi.org/10.1126/science.aav2412>.
- [36] S.M. Kim, P.M. Abdala, T. Margossian, D. Hosseini, L. Foppa, A. Armutlulu, W. Van Beek, A. Comas-Vives, C. Copéret, C. Müller, Cooperativity and dynamics increase the performance of NiFe dry reforming catalysts, *J. Am. Chem. Soc.* 139 (2017) 1937–1949, <https://doi.org/10.1021/jacs.6b11487>.
- [37] T. Zhang, Z. Liu, Y.-A. Zhu, Z. Liu, Z. Sui, K. Zhu, X. Zhou, Dry reforming of methane on Ni-Fe-MgO catalysts: influence of Fe on carbon-resistant property and kinetics, *Appl. Catal. B Environ.* 264 (2020), 118497, <https://doi.org/10.1016/j.apcatb.2019.118497>.
- [38] J. Oh, S. Joo, C. Lim, H.J. Kim, F. Ciucci, J.-Q. Wang, J.W. Han, G. Kim, Precise modulation of triple-phase boundaries towards a highly functional exsolved catalyst for dry reforming of methane under a dilution-free system, *Angew. Chem.* (2022), e202204990, <https://doi.org/10.1002/ange.202204990>.
- [39] D. Neagu, T.-S.S. Oh, D.N. Miller, H. Ménard, S.M. Bukhari, S.R. Gamble, R. J. Gorte, J.M. Vohs, J.T.S. Irvine, Nano-socketed nickel particles with enhanced coking resistance grown in situ by redox exsolution, *Nat. Commun.* 6 (2015) 8120, <https://doi.org/10.1038/ncomms9120>.
- [40] S. Das, J. Ashok, Z. Bian, N. Dewangan, M.H. Wai, Y. Du, A. Borgna, K. Hidajat, S. Kawi, Silica–Ceria sandwiched Ni core–shell catalyst for low temperature dry reforming of biogas: Coke resistance and mechanistic insights, *Appl. Catal. B Environ.* 230 (2018) 220–236, <https://doi.org/10.1016/j.apcatb.2018.02.041>.
- [41] Z. Bian, S. Kawi, Preparation, characterization and catalytic application of phyllosilicate: a review, *Catal. Today* 339 (2020) 3–23, <https://doi.org/10.1016/j.cattod.2018.12.030>.
- [42] T.W. van Deelen, C. Hernández Mejía, K.P. de Jong, Control of metal-support interactions in heterogeneous catalysts to enhance activity and selectivity, *Nat. Catal.* 2 (2019) 955–970, <https://doi.org/10.1038/s41929-019-0364-x>.
- [43] C.M. Marin, E.J. Popczun, T. Nguyen-phan, D.N. Tafen, D. Alfonso, I. Waluyo, A. Hunt, D.R. Kauffman, Designing perovskite catalysts for controlled active-site exsolution in the microwave dry reforming of methane, *Appl. Catal. B Environ.* 284 (2021), 119711, <https://doi.org/10.1016/j.apcatb.2020.119711>.
- [44] X. Gao, J. Ashok, S. Kawi, Smart designs of anti-coking and anti-sintering ni-based catalysts for dry reforming of methane: a recent review, *Reactions* 1 (2020) 162–194, <https://doi.org/10.3390/reactions1020013>.
- [45] X. Gao, W. Lin, Z. Ge, H. Ge, S. Kawi, Modification strategies of ni-based catalysts with metal oxides for dry reforming of methane, *Methane* 1 (2022) 139–157, <https://doi.org/10.3390/methane1030012>.
- [46] X. Gao, Y. Wen, R. Tan, H. Huang, S. Kawi, A review of catalyst modifications for a highly active and stable hydrogen production from methane, *Int. J. Hydrog. Energy* (2022), <https://doi.org/10.1016/j.ijhydene.2022.06.185>.
- [47] D. Neagu, G. Tsekouras, D.N. Miller, H. Ménard, J.T.S. Irvine, In situ growth of nanoparticles through control of non-stoichiometry, *Nat. Chem.* 5 (2013) 916–923, <https://doi.org/10.1038/nchem.1773>.
- [48] O. Kwon, S. Sengodan, K. Kim, H.Y. Jeong, J. Shin, Y.W. Ju, J.W. Han, G. Kim, Exsolution trends and co-segregation aspects of self-grown catalyst nanoparticles in perovskites, *Nat. Commun.* 8 (2017) 1–7, <https://doi.org/10.1038/ncomms15967>.
- [49] S. Sengodan, S. Choi, A. Jun, T.H. Shin, Y.W. Ju, H.Y. Jeong, J. Shin, J.T.S. Irvine, G. Kim, Layered oxygen-deficient double perovskite as an efficient and stable anode for direct hydrocarbon solid oxide fuel cells, *Nat. Mater.* 14 (2015) 205–209, <https://doi.org/10.1038/nmat4166>.
- [50] Y.F. Sun, Y.Q. Zhang, J. Chen, J.H. Li, Y.T. Zhu, Y.M. Zeng, B.S. Amirkhiz, J. Li, B. Hua, J.L. Luo, NeW opportunity for in situ exsolution of metallic nanoparticles on perovskite parent, *Nano Lett.* 16 (2016) 5303–5309, <https://doi.org/10.1021/acs.nanolett.6b02757>.



- [51] P.B. Managutti, S. Tymen, X. Liu, O. Hernandez, C. Prestipino, A. Le Gal La Salle, S. Paul, L. Jalowiecki-Duhamel, V. Dorcet, A. Billard, P. Briois, M. Bahout, Exsolution of Ni nanoparticles from a site-deficient layered double perovskites for dry reforming of methane and as an anode material for a solid oxide fuel cell, *ACS Appl. Mater. Interfaces* 13 (2021) 35719–35728, <https://doi.org/10.1021/acsaami.1c08158>.
- [52] M. Li, B. Hua, Y. Zeng, B. Shalchi Amirkhiz, J.L. Luo, Thermally stable and coking resistant CoMo alloy-based catalysts as fuel electrodes for solid oxide electrochemical cells, *J. Mater. Chem. A* 6 (2018) 15377–15385, <https://doi.org/10.1039/c8ta04749a>.
- [53] S. Joo, A. Seong, O. Kwon, K. Kim, J.H. Lee, R.J. Gorte, J.M. Vohs, J.W. Han, G. Kim, Highly active dry methane reforming catalysts with boosted in situ grown Ni-Fe nanoparticles on perovskite via atomic layer deposition, *Sci. Adv.* 6 (2020) 1–9, <https://doi.org/10.1126/sciadv.abb1573>.
- [54] S. Joo, O. Kwon, S. Kim, H.Y. Jeong, G. Kim, Ni-Fe bimetallic nanocatalysts produced by topotactic exsolution in Fe deposited PrBaMn 1.7 Ni 0.3 O 5+  $\delta$  for dry reforming of methane, *J. Electrochem. Soc.* 167 (2020), 064518, <https://doi.org/10.1149/1945-7111/ab8390>.
- [55] S. Joo, O. Kwon, K. Kim, S. Kim, H. Kim, J. Shin, H.Y. Jeong, S. Sengodan, J. W. Han, G. Kim, Cation-swapped homogeneous nanoparticles in perovskite oxides for high power density, *Nat. Commun.* 10 (2019) 697, <https://doi.org/10.1038/s41467-019-08624-0>.
- [56] S. Joo, K. Kim, O. Kwon, J. Oh, H.J. Kim, L. Zhang, J. Zhou, J. Wang, H.Y. Jeong, J. W. Han, G. Kim, Enhancing thermocatalytic activities by upshifting the d-band center of exsolved Co-Ni-Fe ternary alloy nanoparticles for the dry reforming of methane, *Angew. Chem.* 133 (2021) 16048–16055, <https://doi.org/10.1002/ange.202101335>.
- [57] B. Ravel, M. Newville, Athena, artemis, hephaestus: data analysis for X-ray absorption spectroscopy using IFEFFIT, *J. Synchrotron Radiat.* 12 (2005) 537–541, <https://doi.org/10.1107/S0909049505012719>.
- [58] K. Chen, S. Lo, L. Chang, R. Egerton, J. Kai, J. Lin, F. Chen, Valence state map of iron oxide thinfilm obtained from electron spectroscopy imaging series, *Micron* 38 (2007) 354–361, <https://doi.org/10.1016/j.micron.2006.06.004>.
- [59] S. Das, S. Bhattar, L. Liu, Z. Wang, S. Xi, J.J. Spivey, S. Kawi, Effect of partial Fe substitution in La<sub>0.9</sub>Sr<sub>0.1</sub>NiO<sub>3</sub> perovskite-derived catalysts on the reaction mechanism of methane dry reforming, *ACS Catal.* 10 (2020) 12466–12486, <https://doi.org/10.1021/acscatal.0c01229>.
- [60] C. Liang, P. Zou, A. Nairan, Y. Zhang, J. Liu, K. Liu, S. Hu, F. Kang, H.J. Fan, C. Yang, Exceptional performance of hierarchical Ni-Fe oxyhydroxide@NiFe alloy nanowire array electrocatalysts for large current density water splitting, *Energy Environ. Sci.* 13 (2020) 86–95, <https://doi.org/10.1039/c9ee02388g>.
- [61] J. Lu, Y.-M. Yin, J. Yin, J. Li, J. Zhao, Z.-F. Ma, Role of Cu and Sr in improving the electrochemical performance of cobalt-free Pr 1-x Sr x Fe 1-y Cu y O 3- $\delta$  cathode for intermediate temperature solid oxide fuel cells, *J. Electrochem. Soc.* 163 (2016) F44–F53, <https://doi.org/10.1149/2.0181602jes>.
- [62] A.L. Allred, E.G. Rochow, A scale of electronegativity based on electrostatic force, *J. Inorg. Nucl. Chem.* 5 (1958) 264–268, [https://doi.org/10.1016/0022-1902\(58\)80003-2](https://doi.org/10.1016/0022-1902(58)80003-2).
- [63] T. Margossian, K. Larmier, S.M. Kim, F. Krumeich, C. Müller, C. Copéret, Supported bimetallic NiFe nanoparticles through colloid synthesis for improved dry reforming performance, *ACS Catal.* 7 (2017) 6942–6948, <https://doi.org/10.1021/acscatal.7b02091>.
- [64] H. Fei, J. Dong, Y. Feng, C.S. Allen, C. Wan, B. Voloskiy, M. Li, Z. Zhao, Y. Wang, H. Sun, P. An, W. Chen, Z. Guo, C. Lee, D. Chen, I. Shakir, M. Liu, T. Hu, Y. Li, A. I. Kirkland, X. Duan, Y. Huang, General synthesis and definitive structural identification of MN<sub>4</sub>C<sub>4</sub> single-atom catalysts with tunable electrocatalytic activities, *Nat. Catal.* 1 (2018) 63–72, <https://doi.org/10.1038/s41929-017-0008-y>.
- [65] Z. Du, H. Zhao, S. Yi, Q. Xia, Y. Gong, Y. Zhang, X. Cheng, Y. Li, L. Gu, K. Świerczek, High-performance anode material Sr<sub>2</sub>FeMo<sub>0.65</sub>Ni<sub>0.35</sub>O<sub>6- $\delta$</sub>  with in situ exsolved nanoparticle catalyst, *ACS Nano* 10 (2016) 8660–8669, <https://doi.org/10.1021/acsnano.6b03979>.
- [66] M.C. Biesinger, B.P. Payne, A.P. Grosvenor, L.W.M. Lau, A.R. Gerson, R.S.C. Smart, Resolving surface chemical states in XPS analysis of first row transition metals, oxides and hydroxides: Cr, Mn, Fe, Co and Ni, *Appl. Surf. Sci.* 257 (2011) 2717–2730, <https://doi.org/10.1016/j.apsusc.2010.10.051>.
- [67] J.-W. Yin, Y. Yin, J. Lu, C. Zhang, N.Q. Minh, Z. Ma, Structure and properties of novel cobalt-free oxides Nd x Sr 1-x Fe 0.8 Cu 0.2 O 3- $\delta$  (0.3  $\leq$  x  $\leq$  0.7) as cathodes of intermediate temperature solid oxide fuel cells, *J. Phys. Chem. C* 118 (2014) 13357–13368, <https://doi.org/10.1021/jp500371w>.
- [68] J. Bao, X. Zhang, B. Fan, J. Zhang, M. Zhou, W. Yang, X. Hu, H. Wang, B. Pan, Y. Xie, Ultrathin spinel-structured nanosheets rich in oxygen deficiencies for enhanced electrocatalytic water oxidation, *Angew. Chem.* 127 (2015) 7507–7512, <https://doi.org/10.1002/ange.201502226>.
- [69] A. Tsoukalou, Q. Imtiaz, S.M. Kim, P.M. Abdala, S. Yoon, C.R. Müller, Dry-reforming of methane over bimetallic Ni–M/La<sub>2</sub>O<sub>3</sub> (M = Co, Fe): the effect of the rate of La<sub>2</sub>O<sub>3</sub> formation and phase stability on the catalytic activity and stability, *J. Catal.* 343 (2016) 208–214, <https://doi.org/10.1016/j.jcat.2016.03.018>.
- [70] Z. Bian, I.Y. Suryawinata, S. Kawi, Highly carbon resistant multicore-shell catalyst derived from Ni-Mg phyllosilicate nanotubes@silica for dry reforming of methane, *Appl. Catal. B Environ.* 195 (2016) 1–8, <https://doi.org/10.1016/j.apcatb.2016.05.001>.
- [71] A. Ramirez, K. Lee, A. Harale, L. Gevers, S. Telalovic, B. Al Solami, J. Gascon, Stable high-pressure methane dry reforming under excess of CO<sub>2</sub>, *ChemCatChem* 12 (2020) 5919–5925, <https://doi.org/10.1002/cctc.202001049>.
- [72] S.A. Theofanidis, R. Batchu, V.V. Galvita, H. Poelman, G.B. Marin, Carbon gasification from Fe-Ni catalysts after methane dry reforming, *Appl. Catal. B Environ.* 185 (2016) 42–55, <https://doi.org/10.1016/j.apcatb.2015.12.006>.
- [73] F.De Groot, Multiplet effects in X-ray spectroscopy, *Coord. Chem. Rev.* 249 (2005) 31–63, <https://doi.org/10.1016/j.ccr.2004.03.018>.
- [74] H. Wang, P. Ge, C.G. Riordan, S. Brooker, C.G. Woerner, T. Collins, C.A. Melendres, O. Graudejus, N. Bartlett, S.P. Cramer, Integrated X-ray L absorption spectra. counting holes in Ni complexes, *J. Phys. Chem. B* 102 (1998) 8343–8346, <https://doi.org/10.1021/jp9821026>.
- [75] H. Wang, S. Friedrich, L. Li, Z. Mao, P. Ge, M. Balasubramanian, D.S. Patil, L-edge sum rule analysis on 3d transition metal sites: from d 10 to d 0 and towards application to extremely dilute metallo-enzymes, *Phys. Chem. Chem. Phys.* 20 (2018) 8166–8176, <https://doi.org/10.1039/C7CP06624D>.
- [76] H.J.M. J.D. Pack, Special points for Brillouin-zone integrations, *Phys. Rev. B* 13 (1976) 5188–5192, <https://doi.org/10.1039/c8ta11250a>.
- [77] D.H. Pearson, C.C. Ahn, B. Fultz, White lines and d-electron occupancies for the 3 d and 4 d transition metals, *Phys. Rev. B* 47 (1993) 8471–8478, <https://doi.org/10.1103/PhysRevB.47.8471>.
- [78] V. De Coster, N.V. Srinath, S.A. Theofanidis, L. Pirro, A. Van Alboom, H. Poelman, M.K. Sabbe, G.B. Marin, V.V. Galvita, Looking inside a Ni-Fe/MgAl<sub>2</sub>O<sub>4</sub> catalyst for methane dry reforming via Mössbauer spectroscopy and in situ QXAS, *Appl. Catal. B Environ.* 300 (2022), 120720, <https://doi.org/10.1016/j.apcatb.2021.120720>.
- [79] H.L. Chen, S.Y. Wu, H.T. Chen, J.G. Chang, S.P. Ju, C. Tsai, L.C. Hsu, Theoretical study on adsorption and dissociation of NO<sub>2</sub> molecule on Fe(111) surface, *Langmuir* 26 (2010) 7157–7164, <https://doi.org/10.1021/la904233b>.
- [80] Y. Chen, J. Yang, Y. Sun, M. Chen, A density functional study of the adsorption of CO on Fe (111) surface, *Chem. J. Internet* 6 (2004) 1–6.
- [81] L. Foppa, M. Silaghi, K. Larmier, A. Comas-vives, Intrinsic reactivity of Ni, Pd and Pt surfaces in dry reforming and competitive reactions: insights from first principles calculations and microkinetic modeling simulations, *J. Catal.* 343 (2016) 196–207, <https://doi.org/10.1016/j.jcat.2016.02.030>.
- [82] Z. Wang, X.M. Cao, J. Zhu, P. Hu, Activity and coke formation of nickel and nickel carbide in dry reforming: a deactivation scheme from density functional theory, *J. Catal.* 311 (2014) 469–480, <https://doi.org/10.1016/j.jcat.2013.12.015>.